

RESEARCH ARTICLE | MAY 01 2004

A comparative study of the turbulent Rayleigh–Taylor instability using high-resolution three-dimensional numerical simulations: The Alpha-Group collaboration

Guy Dimonte; D. L. Youngs; A. Dimits; S. Weber; M. Marinak; S. Wunsch; C. Garasi; A. Robinson; M. J. Andrews; P. Ramaprabhu; A. C. Calder; B. Fryxell; J. Biello; L. Dursi; P. MacNeice; K. Olson; P. Ricker; R. Rosner; F. Timmes; H. Tufo; Y.-N. Young; M. Zingale



Physics of Fluids 16, 1668–1693 (2004)

<https://doi.org/10.1063/1.1688328>



View
Online



Export
Citation

Articles You May Be Interested In

Density ratio dependence of Rayleigh–Taylor mixing for sustained and impulsive acceleration histories

Physics of Fluids (February 2000)

Two-phase flow analysis of unstable fluid mixing in one-dimensional geometry

Physics of Fluids (October 2000)

A comparative study of the turbulent Rayleigh–Taylor instability using high-resolution three-dimensional numerical simulations: The Alpha-Group collaboration

Guy Dimonte

Los Alamos National Laboratory, Los Alamos, New Mexico 87545

D. L. Youngs

Atomic Weapons Establishment, Aldermaston, Reading, Berkshire RG7 4PR, United Kingdom

A. Dimits, S. Weber, and M. Marinak

Lawrence Livermore National Laboratory, Livermore, California 94551

S. Wunsch

Sandia National Laboratories, Livermore, California 94551

C. Garasi and A. Robinson

Sandia National Laboratories, Albuquerque, New Mexico 87185-0819

M. J. Andrews and P. Ramaprabhu

Texas A & M University, College Station, Texas 77843-3123

A. C. Calder, B. Fryxell, J. Biello, and L. Dursi

University of Chicago, Chicago, Illinois 60637

P. MacNeice and K. Olson

NASA Goddard Space Flight Center, Greenbelt, Maryland 20771

P. Ricker, R. Rosner, F. Timmes, H. Tufo, Y.-N. Young, and M. Zingale

University of Chicago, Chicago, Illinois 60637

(Received 2 May 2003; accepted 29 January 2004; published online 8 April 2004)

The turbulent Rayleigh–Taylor instability is investigated in the limit of strong mode-coupling using a variety of high-resolution, multimode, three dimensional numerical simulations (NS). The perturbations are initialized with only short wavelength modes so that the self-similar evolution (i.e., bubble diameter $D_b \propto$ amplitude h_b) occurs solely by the nonlinear coupling (merger) of saturated modes. After an initial transient, it is found that $h_b \sim \alpha_b A g t^2$, where A =Atwood number, g =acceleration, and t =time. The NS yield $D_b \sim h_b/3$ in agreement with experiment but the simulation value $\alpha_b \sim 0.025 \pm 0.003$ is smaller than the experimental value $\alpha_b \sim 0.057 \pm 0.008$. By analyzing the dominant bubbles, it is found that the small value of α_b can be attributed to a density dilution due to fine-scale mixing in our NS without interface reconstruction (IR) or an equivalent entrainment in our NS with IR. This may be characteristic of the mode coupling limit studied here and the associated α_b may represent a lower bound that is insensitive to the initial amplitude. Larger values of α_b can be obtained in the presence of additional long wavelength perturbations and this may be more characteristic of experiments. Here, the simulation data are also analyzed in terms of bubble dynamics, energy balance and the density fluctuation spectra. © 2004 American Institute of Physics. [DOI: 10.1063/1.1688328]

I. INTRODUCTION

The Rayleigh–Taylor (RT) instability^{1,2} occurs when a low density (ρ_l) fluid accelerates a high density (ρ_h) fluid or, equivalently, when the “light” fluid supports the “heavy” fluid against gravity. An interfacial perturbation grows exponentially^{3,4} until its amplitude becomes comparable to its wavelength λ . Then, the perturbation becomes asymmetric with the asymmetry increasing with the Atwood number $A \equiv (\rho_h - \rho_l)/(\rho_h + \rho_l)$. The “light” fluid penetrates the “heavy” fluid as bubbles with a terminal velocity $\propto \sqrt{\lambda}$ for a single mode.^{4–20} If the unstable spectrum is broad, then successively larger bubbles rise to the front^{10,20} and the charac-

teristic wavelength of the dominant bubbles λ_b grows with their amplitude h_b . For a constant acceleration $gA > 0$, the growth is self-similar ($\lambda_b \propto h_b$) with^{19–55}

$$h_b = \alpha_b A g t^2. \quad (1)$$

The “heavy” fluid penetrates the “light” fluid as spikes, similar to bubbles at $A \ll 1$. However, as A approaches 1, the spikes become narrow and approach free fall $\Rightarrow g t^2/2$.

Equation (1) can be ascertained from simple bubble dynamics when the bubble diameter D_b grows self-similarly with h_b . In particular, a single bubble is found to rise with a terminal velocity^{5–16}

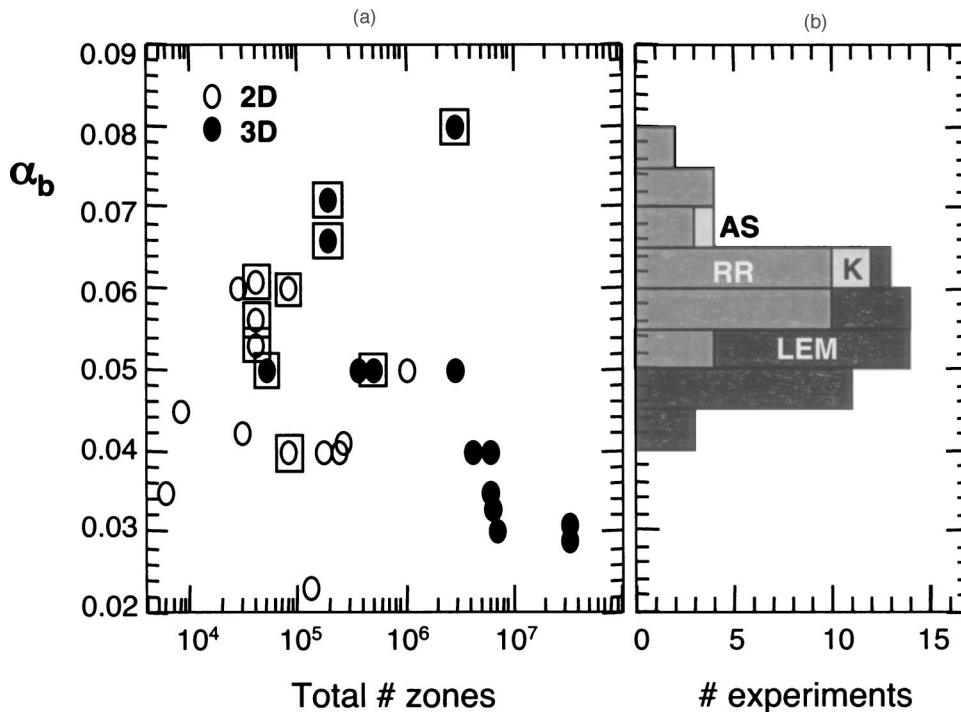


FIG. 1. (a) α_b vs total number of zones from previously published simulations. Squares indicate simulations with interface reconstruction. (b) Histogram from previous experiments.

$$V_b = \text{Fr} \sqrt{\frac{\delta\rho}{\rho_h} \frac{g D_b}{2}}, \quad (2)$$

where $\delta\rho = \rho_h - \rho_l$ if there is no entrainment, and Fr is a constant ($\sim \sqrt{\text{Froude \#}}$). If $D_b \propto h_b$, Eq. (2) is solved by Eq. (1) with

$$\alpha_b = \frac{\text{Fr}^2}{8} \frac{D_b}{h_b} \frac{\Sigma\rho}{\rho_h}, \quad (3)$$

where $\Sigma\rho \equiv \rho_h + \rho_l$. In this picture, the key factors determining α_b are Fr, D_b/h_b , and, implicitly, $\delta\rho$. If there is significant diffusion or entrainment into the bubbles as they traverse the mixing layer, the density contrast will be reduced so that $\delta\rho < \rho_h - \rho_l$ and the effective Atwood number is $\delta\rho/\Sigma\rho < A$.

The bubbles can grow self-similarly in two limiting ways. In one limit, the ambient perturbations grow exponentially and independently until they transition to their terminal velocity when h_b becomes comparable to λ_b . This produces a series of saturated modes at successively longer wavelength with α_b and λ_b/h_b increasing weakly with the initial amplitudes.^{20,21,34,49,50} In the opposite limit, the bubbles are taken to merge to larger and faster bubbles.^{16,17,32,44-48} Since this involves the nonlinear coupling of newly saturated modes with “intrinsic” scales $h_b \sim \lambda_b$, the resultant α_b is thought to be insensitive to the initial conditions.²³

A historical survey of α_b from experiments and numerical simulations (NS) is shown in Fig. 1. The “rocket rig” (RR) experiments^{24,25} with $g \sim 30 g_0$ ($g_0 = 980 \text{ cm/s}^2$) and a variety of immiscible liquids verified Eq. (1) with $\alpha_b \sim 0.063 \pm 0.007$ independent of A . Experiments by Kucherenko *et al.* (K) (Ref. 27) obtained $\alpha_b \sim 0.063$ at $A = 0.5$ and 0.9, and Andrews and Spalding (AS) (Ref. 26) obtained $\alpha_b \sim 0.07$ at $A \ll 1$. A comprehensive variation of A

on the Linear Electric Motor (LEM) (Ref. 30) yielded $\alpha_b \sim 0.05 \pm 0.005$ when surfactants were used to reduce the surface tension ($\alpha_b \Rightarrow 0.06$ without surfactants). In addition, the leading bubbles were analyzed at various A to obtain a self-similarity ratio of $D_b/h_b \sim 0.54 \pm 0.07 \rho_h/\Sigma\rho$. The first NS (Refs. 23, 25, 31, 35, 36, 38, 39) conducted in two dimensions (2D) without front-tracking (FT) obtained $\alpha_b \sim 0.035-0.05$. Larger values of α_b were expected in 3D since single modes grow faster (larger Fr) than in 2D. Instead, the highest resolution 3D simulations^{35,38-42} obtained $\alpha_b \sim 0.03$. Simulations with FT obtained larger values $\alpha_b \sim 0.05-0.08$ in both 2D (Refs. 32, 33, 48) and 3D (Refs. 14, 17, 43, 44), and this was associated with the reduction in numerical diffusion. However, Glimm *et al.*³² also reported that α_b decreased to as small as 0.038 late in time as the bubble “connectivity” (entrainment) increased. When entrainment was reduced in the LEM (Ref. 30) by increasing the surface tension 50-fold, α_b increased by 20%. Unfortunately, this also imposed long wavelength initial perturbations and these can also increase α_b .^{21,22,31,34,40,49} Although these various results can be confusing, they do suggest that entrainment and the initial conditions can affect the value of α_b .

In this paper, we investigate some of these issues by comparing a variety of multimode RT simulations quantitatively. We consider only the limit that is dominated by mode-coupling because the resulting α_b is thought to be insensitive to initial conditions. This is accomplished by imposing only short wavelength perturbations so that long wavelength modes are generated solely by nonlinear mode-coupling. The NS appear to be converged since we obtain similar results with different zoning: $128 \times 128 \times 256$ and $256 \times 256 \times 512$. The main emphasis is on the mixing of miscible fluids (low Schmidt number) at high Reynolds number in which a

Kolmogorov-type spectrum is expected with significant dissipation in energy and density fluctuations. However, subzone mixing reduces the density contrast and this raises the concern that, in the simulations without interface reconstruction (IR), entrainment may be overestimated due to excessive numerical diffusion. Hence, we compare NS with and without IR. With IR, subzone mixing is reduced significantly but it is replaced by an equivalent small-scale entrainment so that α_b remains the same. This may be characteristic of the mode-coupling limit since mode-coupling produces both shorter and longer wavelength modes and the former promotes entrainment and diffusion. The rest of the paper is organized as follows.

We first describe the codes in Sec. II. Then, in Sec. III, we evaluate the codes with single mode studies at different resolutions particularly since the imposed modes are near the resolution limit. The exponential growth rate at small amplitude is compared with analytical solutions to ascertain the effective numerical viscosity for short wavelength modes. The terminal velocity at large amplitude is then used to obtain Fr for periodic modes and this is compared with potential flow theory.^{10–12}

Section IV describes the multimode results. The amplitudes are found to obey Eq. (1) with very good agreement among the NS in most physical quantities including the asymptotic values of α_b . However, the calculated α_b are 40% smaller than observed experimentally and this is important because α_b is used to calibrate mix models.^{25,31,46–57}

To clarify the difference in α_b and to further evaluate the NS, the dominant bubbles are analyzed in terms of the expected self-similar dynamics in Sec. V. In particular, we verify self-similarity by calculating the characteristic diameter of the dominant bubbles D_b using the autocorrelation of the bubble front. We also calculate the average density of the dominant bubbles and find that it is $\rho_b \sim 2\rho_l$ due to diffusion without IR or entrainment with IR. When ρ_b is used instead of ρ_l in $\delta\rho$ in Eq. (2), we find that the leading bubbles have an $Fr \sim 1$ consistent with RT experiments^{7,30,46,49} and single plumes.⁸ Similalry, if ρ_b is used to calculate an effective Atwood number $(\rho_h - \rho_b)/(\rho_h + \rho_b) \sim 0.2$ in Eq. (1), then the effective $\alpha_b \sim 0.06$ is more like the experiments.

Section VI contains an analysis of the kinetic, potential and dissipated energies. For $A \ll 1$, α_b is found to be proportional to the kinetic/potential energies. Then, by energy conservation, the low value of α_b in the NS is consistent with the dissipated energy which is $\sim 50\%$ of the converted potential energy. This can also be related to the dissipation of density fluctuations as described previously.

In Sec. VII, the volume fraction fluctuations are characterized by their Fourier power spectrum and found to obey a Kolmogorov-type spectrum with an inertial range given by D_b . The dissipation scale is found to agree with the Kolmogorov wavelength calculated with the numerical viscosity obtained from the single mode studies.

Finally, the results are summarized in Sec. VIII. The substantial agreement among the NS (with and without IR) and with analytical linear and nonlinear bubble dynamics indicate that the numerical results are reasonable. This is supported by the spectral analysis that suggests that over

TABLE I. Code types and names.

Institution	Code	Method	Zoning	IR
AWE	TURMOIL3D	Eulerian	256×256×512	No
			128×128×256	No
U. Chicago	FLASH	P-P-M	256×256×512	No
LLNL	WP/PPM	P-P-M	256×256×512	No
LLNL	NAV/STK	N-S	256×256×512	No
Texas A & M	RTI-3D	Eulerian	128×128×256	No
LLNL	HYDRA	ALE	256×256×512	No
			128×128×256	Yes and No
Sandia NL	ALEGRA	ALE	128×128×256	Yes and No

90% of the fluctuations are resolved late in time. As a result, the discrepancy in α_b between NS and experiments may be attributable other physical attributes such as differences in the initial perturbations.

II. NUMERICAL SIMULATIONS (NS) AND CONFIGURATION

A. Properties of NS

This comparative study is performed with seven codes from five different institutions as summarized in Table I. The Eulerian type codes TURMOIL3D, FLASH, WP/PPM, NAV/STK, and RTI-3D do not have interface reconstruction (IR), whereas the ALE codes HYDRA and ALEGRA have IR capability. All are forms of monotone-integrated large-eddy simulations (MILES) such as described in Ref. 59. MILES techniques are favored for our RT test case because the Monotonic numerical methods are able to treat the initial density discontinuity without generating spurious oscillations. The multimode NS are conducted with two zone configurations: 128 × 128 × 256 and 256 × 256 × 512. The TURMOIL3D and HYDRA simulations are conducted in both zone configurations for a more direct comparison. Since IR is computationally intensive, they have only been conducted with the coarser zoning.

It should also be pointed out that the compressible codes (all except RTI-3D) conserve the mass fraction in order to cast the evolution equations in conservative form. The volume fraction is inferred from the mass fraction using pressure balance in each zone and is not strictly conserved. This may introduce an error in our bubble and spike amplitudes since they are determined from the volume fraction because it is useful near $A = 1$ (and to compare with incompressible NS). Here, this error should be small because our test problem is nearly incompressible.

1. TURMOIL3D

TURMOIL3D is a compressible Eulerian code which uses the explicit numerical method of Youngs⁶⁰ on a staggered Cartesian grid. The interface tracking method described in Ref. 60 is not used. Instead, an additional equation is solved for the advection of the mass fraction of one of the fluids. The calculation for each time step is divided into two phases. First, the Lagrangian phase advances the velocity and internal energy by solving the Euler equations using a second-order-accurate nondissipative time integration technique. In the absence of gravity this conserves the sum of kinetic plus

internal energy. In the second phase, the fluxes across cell boundaries are calculated for all fluid variables by using the third-order-accurate monotonic advection method of van Leer.⁶¹ Operator splitting is used in X , Y and advection in Z is calculated in separate steps. The monotonicity constraints in the advection phase give sufficient dissipation of velocity and concentration fluctuations at high wave number to make an explicit sub-grid-scale model unnecessary. The advection phase conserves mass, internal energy and momentum but the kinetic energy is dissipated. The dissipation in each cell for each time step is calculated using the formula of DeBar⁶² and added to the internal energy. Hence the DeBar formula gives a direct estimate of the sub-grid-scale energy dissipation.

2. FLASH

FLASH is an adaptive-mesh compressible hydrodynamics code developed for astrophysical flows. The hydrodynamics module solves Euler's equations using the Piecewise Parabolic Method (PPM).⁶³ The PPM scheme uses parabolas to interpolate between zones on a Cartesian grid in order to better represent smooth spatial gradients than linear interpolation schemes. Mesh adaptivity is handled by the PARAMESH library,⁶⁴ which utilizes a block-structured grid organized by a tree structure. FLASH is designed for massively-parallel distributed memory architectures, and uses the Message Passing Interface⁶⁵ for portability. A complete description of the code including the results of test calculations is given in Fryxell *et al.*,⁶⁶ and the results of performance tests are discussed in Calder *et al.*⁶⁷

3. WP/PPM

This code uses a version of PPM described by Woodward and Porter⁶⁸ that is a higher-order extension of Godunov's method⁶⁹ of a type first introduced by van Leer⁷⁰ but with a MUSCL algorithm that is better suited for strong shocks. The compressible Euler equations are evolved using a procedure that is directionally split and entails taking a Lagrangian step followed by a remap onto the original Cartesian grid. This introduces an intrinsic dissipation for scales comparable to the zone size.

4. Navier–Stokes (NAV/STK)

The NAV/STK code is similar to the WP/PPM code described above but with an explicit physical viscosity

$$v \sim 0.21 \sqrt{Ag\Delta^3}. \quad (4)$$

In addition, there is a thermal conduction with the thermal diffusivity equal to the kinematic viscosity.

5. RTI-3D

RTI-3D is an incompressible 3D code described by Andrews.⁷¹ The code is third order accurate and uses van Leer⁶¹ limiters for advection of momentum and scalars to prevent nonphysical oscillations. Volume-fractions are used to mark the different density fluids and a conjugate gradient/multigrid method is used to solve a Poisson equation for pressure corrections.

6. HYDRA

HYDRA (Ref. 72) is a radiation hydrodynamics code with arbitrary Lagrange Eulerian (ALE) capability. The hydrodynamics equations have an artificial viscosity to stabilize shocks and are solved during the Lagrange phase using a predictor–corrector time integration. This is followed by an advection phase that uses a modified vanLeer method. The code can be used with and without interface reconstruction (Ref. 60, p. 273) to resolve different materials.

7. ALEGRA

The ALEGRA (Arbitrary-Lagrangian-Eulerian General Research Applications) code is Sandia's next-generation, large-deformation, shock-physics code. The code uses an ALE formulation on an unstructured mesh as described in Ref. 73. The user may choose whether to run the code in a purely Eulerian mode (stationary mesh), purely Lagrangian mode (comoving mesh and fluid), or an arbitrary combination of the two. The RT simulations presented here were run in the purely Eulerian mode, using a simple Cartesian but formally unstructured mesh. For such hydrodynamic instability problems, the code has two options for mixing the two fluids. One is to permit the two fluids to mix via numerical diffusion, resulting in intermediate densities in cells containing both fluids. The other is to use an interface reconstruction scheme to keep the fluids separate, resulting in some cells containing both fluids with an approximate “surface” separating them. The IR scheme used in ALEGRA is a modified version of an algorithm created by Youngs.⁷⁴

B. Initial equilibrium and perturbations

The computational domain is a 3D box with horizontal widths $L = 10$ cm in X and Y and height $2L$ in Z . A vertical slice and density profile are shown in Fig. 2. The hydrostatic equilibrium is chosen to be adiabatic

$$\rho = \rho_0 \left(1 - \frac{\gamma-1}{\gamma} \frac{\rho_0 g z}{P_0} \right)^{1/(\gamma-1)} \quad (5)$$

with $\rho_0 = \rho_h$ for $Z > 0$ and $\rho_0 = \rho_l$ for $Z < 0$ and an ideal gas constant $\gamma = 5/3$. The present NS are performed in a nearly incompressible regime by choosing $P_0 = 2\pi(\rho_h + \rho_l)gL = 500$ dyn/cm² to conform with most previous experiments and to limit the vertical density variation (<6%). The effective density contrast (and A) is even more constant in the adiabatic equilibrium because bubbles (spikes) expand (contract) as they rise (fall) in the adiabatic atmosphere. These conditions keep A nearly constant as the mixing region grows. Of course, there is a significant penalty for working in such an incompressible regime because the Courant time step is small.

The initial perturbations are defined as modal amplitudes and they are used to distort the mesh in HYDRA. In FLASH, they are converted to velocity perturbations using linear theory and applied to a square mesh. In the remaining codes, the initial mesh is square and the amplitudes are converted to equivalent density perturbations in the horizontal planes above ($\rho_h h_0 / \Delta$ for $h_0 > 0$) and below ($h_0 < 0$ as $\rho_l h_0 / \Delta$) the interface, where Δ is the zone width.

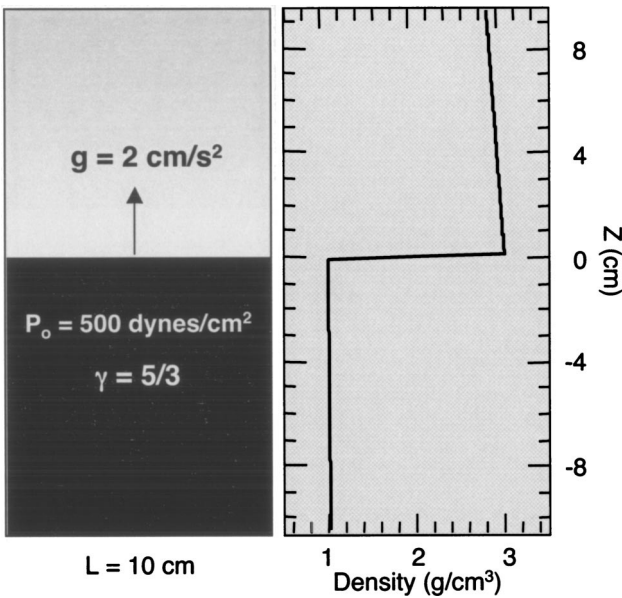


FIG. 2. Initial vertical density profile for 3D box of width L and height $2L$ filled with ideal gases of specific heat ratio γ , initial interface pressure P_0 and acceleration g .

Throughout this paper, we use a nomenclature for each case that starts with the letter S for single mode simulations and M for multimode simulations. This is followed by three digits representing the number of transverse zones per side. The geometry is 3D with a square cross section of width L and a height of $2L$. For example, a single mode NS with a zoning of $16 \times 16 \times 32$ is called S016 and a multimode NS with $256 \times 256 \times 512$ is called M256. The initial conditions for each NS is described separately.

III. SINGLE-MODE STUDIES

Single mode calculations in 3D are used to evaluate the NS by comparing the results with analytical solutions as the zone width Δ is varied. At small amplitude, the exponential growth rate is compared with its theoretical value with viscosity to infer an effective numerical viscosity. At large amplitude, the NS are used to calculate the single bubble terminal velocity to infer Fr, which is then compared to the potential flow result. In bubble models, Fr is directly relevant to α_b .

The single mode NS were performed with the same hydrostatic equilibrium described in Sec. II B and a square-mode initial perturbation

$$h_0(\text{cm}) = 0.01[\cos(kx) + \cos(ky)] \quad (6)$$

with $\lambda = 10 \text{ cm}$. The bubble and spike amplitudes are calculated by interpolating for the 50% volume fraction contour. The evolution of the bubble amplitude and velocity is exemplified for HYDRA in Figs. 3(a) and 3(b) for $\lambda/\Delta = 4, 8, 16$, and 32. The solid lines are without IR and the symbols are with IR, both with the same color coding. The initial growth at small amplitude follows $\cosh(\Gamma t)$ as expected from linear theory and it is used to infer (by fitting) the exponential growth rate Γ . Then, at large amplitude, the bubble transitions continuously to a nearly constant velocity which is

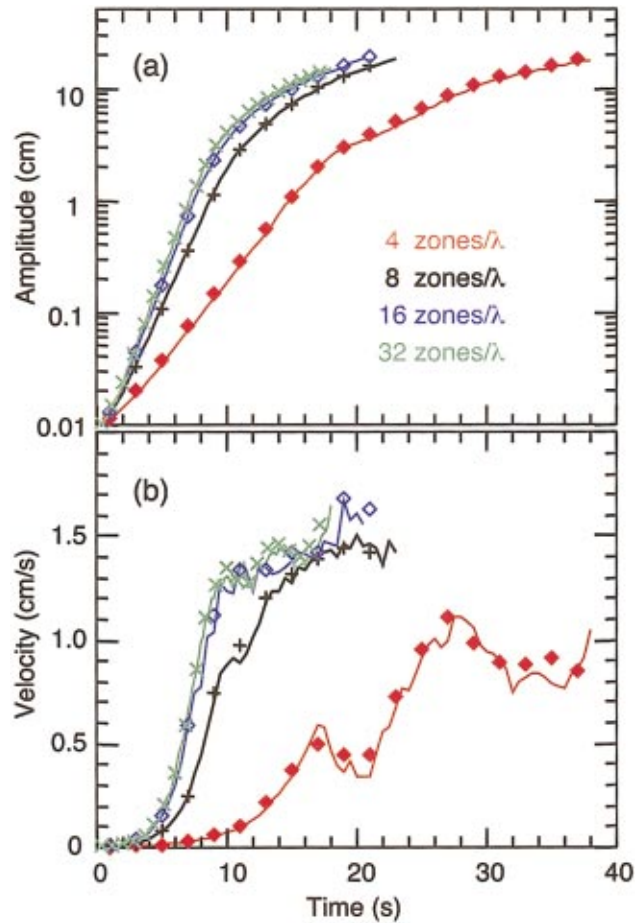


FIG. 3. (Color) Temporal evolution of 3D single modes for various zoning from HYDRA. (a) Amplitude and (b) bubble velocity. Lines are without interface reconstruction (IR) and symbols are with IR.

compared to Eq. (2) to infer Fr. All codes exhibit reduced Γ and Fr as the numerical resolution is degraded.

The variation of Γ with resolution ($k\Delta$) is shown in Fig. 4(a). When scaled to the classical growth rate $\sqrt{Ak}g$, Γ is seen to decrease with $k\Delta$ (as the resolution decreases). Here, this is attributed to a numerical viscosity by fitting the NS results to the RT dispersion relation (dotted line) given by Eq. (121) of Chandrasekhar.³ For $A \sim 1$, Eq. (121) reduces to⁷⁵

$$\Gamma^2 - Ak^2 \Gamma + 4k^4 v^2 (\sqrt{1 + \Gamma/k^2 v} - 1) = 0. \quad (7)$$

For smaller A , the solution to Chandrasekahr's Eq. (121) differs from that to our Eq. (7) by <3%. We scale the kinematic viscosity

$$v \sim \varpi \sqrt{Ag \Delta^3} \quad (8)$$

with a coefficient ϖ that is varied [lines in Fig. 4(a)] to fit the growth rates from each code. We find $0.18 \leq \varpi \leq 0.51$ as summarized in Table II. The accuracy of this method is exemplified by WP/PPM ($\varpi \sim 0.28$) and NAV/STK ($\varpi \sim 0.53$) because the latter is identical to the former except with an explicit viscosity (and thermal diffusivity) given by Eq. (4). The difference between the WP/PPM and NAV/STK results $\delta\varpi \sim 0.25$ is similar to the additional physical viscosity $\varpi \sim 0.21$. The 20% discrepancy is a reasonable uncertainty in the viscosity

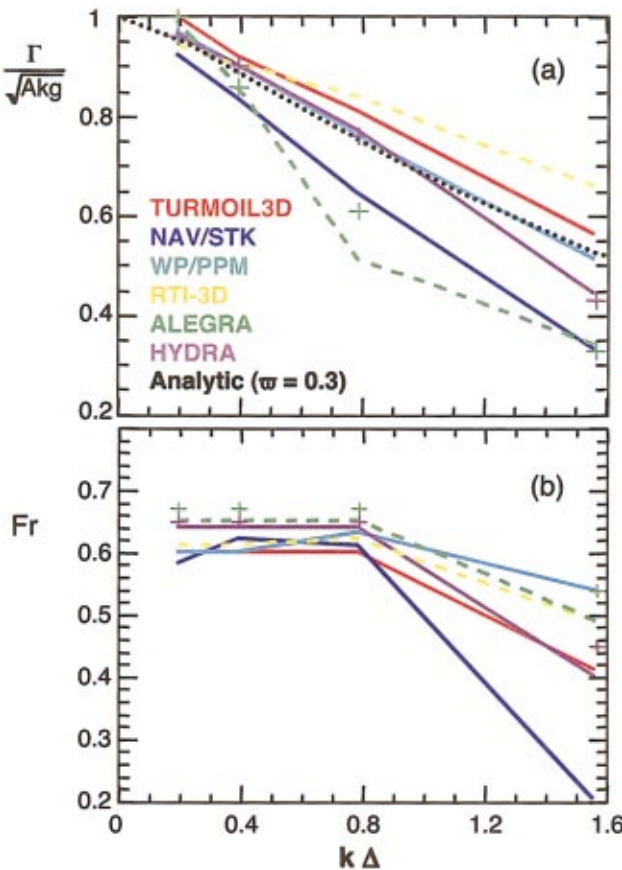


FIG. 4. (Color) (a) Scaled exponential growth rate and (b) bubble Froude-type number Fr vs $k\Delta$, where Δ =zone size.

using this method. It should be noted that the numerical dissipation in second order techniques are nonlinear and our inferred viscosity may be most applicable at short wavelengths.

At large amplitude, the terminal bubble velocity is characterized by Fr in Fig. 4(b) and Table II for each code. To obtain Fr using Eq. (2), it is first necessary to relate the bubble diameter D_b to the periodicity wavelength λ_b , which must include the spike width. The spike is similar to the bubble at $A=0$ by symmetry so that $\lambda_b \sim 2D_b$ and relatively narrow at $A=1$ because it is in free fall so that $\lambda_b \sim D_b$. For intermediate A , Daly⁷⁶ suggested the simple relation

TABLE II. Single mode viscosity coefficient ϖ in Eq. (8) and Fr using Eq. (23).

Simulation	ϖ	Fr
TURMOIL3D	0.23	0.60
FLASH		
NAV/STK	0.53	0.60
WP/PPM	0.28	0.60
RTI-3D	0.22	0.61
ALEGRA	0.50	0.65
ALEGRA_IR	0.45	0.67
HYDRA	0.31	0.64
HYDRA_IR	0.31	0.65
Average	0.35 ± 0.12	0.63 ± 0.03

$$\lambda_b \sim D_b \frac{\rho_h + \rho_l}{\rho_h}. \quad (9)$$

With this substitution, Eq. (2) becomes

$$V_b = Fr \sqrt{A g \lambda_b / 2} \quad (10)$$

which has been used in previous single mode NS.⁴⁹ Fr is inferred from Eq. (10) using the terminal velocity at large amplitude such as that shown in Fig. 3(b). As with Γ , Fr is found to decrease with $k\Delta$, but it converges much faster than Γ . This may be due to the fact that more vertical zones are utilized in the nonlinear phase since $h_b > \lambda_b$.

IV. MULTIMODE SIMULATIONS

The multimode study is initialized with perturbations designed to investigate the self-similar RT instability when dominated by mode coupling. This limiting case is expected to be the least sensitive to initial conditions because it involves the nonlinear coupling of saturated high- k modes of intrinsic scales $h \sim 1/k$. To assure that the low- k modes are generated exclusively by mode coupling, the initial perturbations are chosen to have finite amplitudes only in an annular shell in k -space at the largest resolvable wave numbers, namely, modes 32–64 for the M256 configuration and 16–32 for M128.

A. Initial perturbations

The initial interface perturbations are taken to be

$$h_0(x, y) = \sum_{k_x, k_y} a_k \cos(k_x x) \cos(k_y y) + b_k \cos(k_x x) \sin(k_y y) + c_k \sin(k_x x) \cos(k_y y) + d_k \sin(k_x x) \sin(k_y y), \quad (11)$$

with a rms amplitude $h_0 \text{ rms} \sim 3 \times 10^{-4} L$. The amplitude profile $h_0(x, y)$ is shown in false color in Fig. 5(a) on a zonal basis. The full image is used for M256 and only the lower left quadrant is used for M128, but both represent $L = 10$ cm. The corresponding spectral amplitudes a_k , b_k , c_k , d_k are chosen randomly within an annulus as shown in Fig. 5(b) ($k=0$ in image center). However, as seen in Fig. 5(c), M256 is finite only between modes 32–64 with average amplitude $\sim 5 \times 10^{-6} L$, whereas M128 is comprised mainly of modes 16–32 with amplitude $\sim 10^{-5} L$.

The initial amplitudes were converted to velocity perturbations in FLASH by applying linear theory on a mode by mode basis, namely,

$$h_0(x, y) = \sum_{k_x, k_y} \Gamma(k) [a_k \cos(k_x x) \cos(k_y y) + b_k \cos(k_x x) \sin(k_y y) + c_k \sin(k_x x) \cos(k_y y) + d_k \sin(k_x x) \sin(k_y y)]. \quad (12)$$

Of course, linear theory is applicable since a_k , b_k , c_k , $d_k \ll 1/k$.

The evolution of the mixing zone is exemplified in Fig. 6 with the isosurfaces of $f_h = 0.99$ (volume fraction of “heavy”

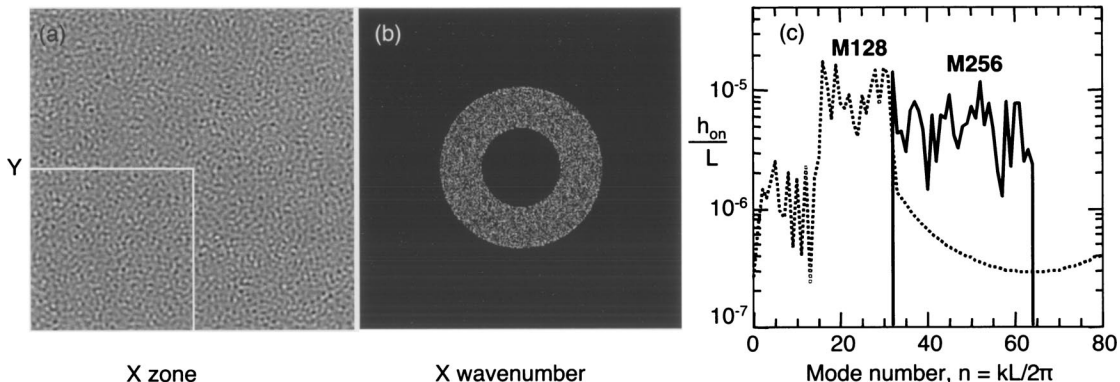


FIG. 5. Initial perturbations in (a) physical and (b) wave number space. (c) Lineouts along X -axis for M256 (solid) and M128 (dotted). Root mean square amplitude is $3 \times 10^{-4} L$.

fluid) from TURMOIL3D at $Ag t^2/L = 5$ and 22. In the early time, there are many bubbles but they already have larger wavelengths than the imposed modes. As they penetrate further, the bubbles increase in size as would be expected from self-similarity. In the following, we analyze the 3D data fields from each NS to quantify the growth rate, self-similarity, molecular mixing, energy dissipation, and fluctuation spectra to compare the NS with each other, experiments and dynamic bubble models.

B. Species concentration (volume fraction) profiles

The fluid interpenetration is characterized in terms of the species concentration or volume fraction of the “heavy” fluid f_h averaged in the spanwise direction

$$\langle f_h \rangle = \int \int f_h dx dy / L^2. \quad (13)$$

The bubble and spike amplitudes h_b and h_s are defined by the Z-location of the $\langle f_h \rangle = 99\%$ and 1% points, respectively, relative to the interface. Vertical profiles of $\langle f_h \rangle$ are shown in Fig. 7 for (a) early and (b) late times. The colored lines from simulations are in good agreement with each other and the gray points are taken from LIF images on the LEM at $A = 0.32$. When normalized to h_b , the early and late profiles are similar indicating that the evolution is self-similar. The profiles are nearly linear and symmetric characteristic of low A with $h_s/h_b \sim 1.17$.

Since h_b and h_s can be subject to statistical fluctuations particularly late in time when there are few bubbles, Andrews and Spalding²⁶ defined the integral mixing width

$$W \equiv \int \langle f_h \rangle \langle f_l \rangle dz \quad (14)$$

which measures the overlap of the heavy $\langle f_h \rangle$ and light $\langle f_l \rangle$ fluids where $f_h + f_l = 1$. For a linear symmetric profile characteristic of $A \sim 0$, one finds $W/h_b = 1/3$. The simulation profiles in Fig. 7 yield $W/h_b \sim 0.31$ in reasonable agreement with $W/h_b \sim 0.33$ for the LEM experiments.³⁰

C. Amplitude evolution

The evolution of W , h_s , h_b is compared with the expected self-similar form of Eq. (1) in Figs. 8–10, respectively.

The solid and dashed lines represent the M256 and M128 simulations without interface reconstruction (IR). Only the M128 simulations were performed with IR because IR is computationally intensive. They are represented as + signs with the same color coding as the NS without IR. The gray points represent LEM experiments taken from laser images at $A = 0.32$ for W and also with backlit photography at $A \sim 0.3$ –0.5 for h_b and h_s .

The amplitudes and displacement are normalized to the other natural lengths in the problem to compare with experiments over a similar dynamic range of scales or (turbulent) regimes. Two scales that represent the limits in the problem are the box width L and the initial dominant wavelength λ_0 . The dominant initial mode λ_0 is important because it is first to grow exponentially and saturate nonlinearly. This begins the self-similar evolution toward longer wavelength and λ_b/λ_0 is indicative of the total number of bubble merger generations.³² The box width is important because it defines the maximum possible wavelength. When λ_b grows to L , the self-similar evolution with $h_b \propto t^2$ ceases and the bubble coasts at the terminal velocity Eq. (9) so that $h_b \propto \sqrt{AgL}t$. Thus, L/λ_0 defines the dynamic range of scales over which self-similar evolution can occur in any given system. This is similar to using the Reynolds number Re to characterize a RT flow since $L/\lambda_0 \sim Re^{2/3}/4\pi$ when λ_0 is determined by viscosity [see Eq. (15) below]. However, L/λ_0 is a more general characterization than Re because it can be applied when λ_0 is determined by any physical attribute like surface tension (RR, LEM), ablation flow (laser fusion) or viscosity.

In the NS, the most unstable mode is found by solving Eq. (7) with the numerical viscosity of Eq. (8). This yields^{3,75}

$$k_p \sim 0.5 \left(\frac{Ag}{v^2} \right)^{1/3} \sim \frac{0.5}{\varpi^{2/3} \Delta} \quad (15)$$

with a peak growth rate

$$\Gamma(k_p) \sim 0.65 \sqrt{Ak_p g}. \quad (16)$$

For the average value in the NS $\varpi \sim 0.35 \pm 0.12$, Eq. (15) implies that the most unstable mode is 40 for M256 and 20 for M128. These modes lie well within the annular initial spectrum and correspond to $\lambda_p = 2.5$ mm for M256 and 5 mm for M128 with $\Gamma \sim 3.3 \text{ s}^{-1}$ and 2.3 s^{-1} , respectively.

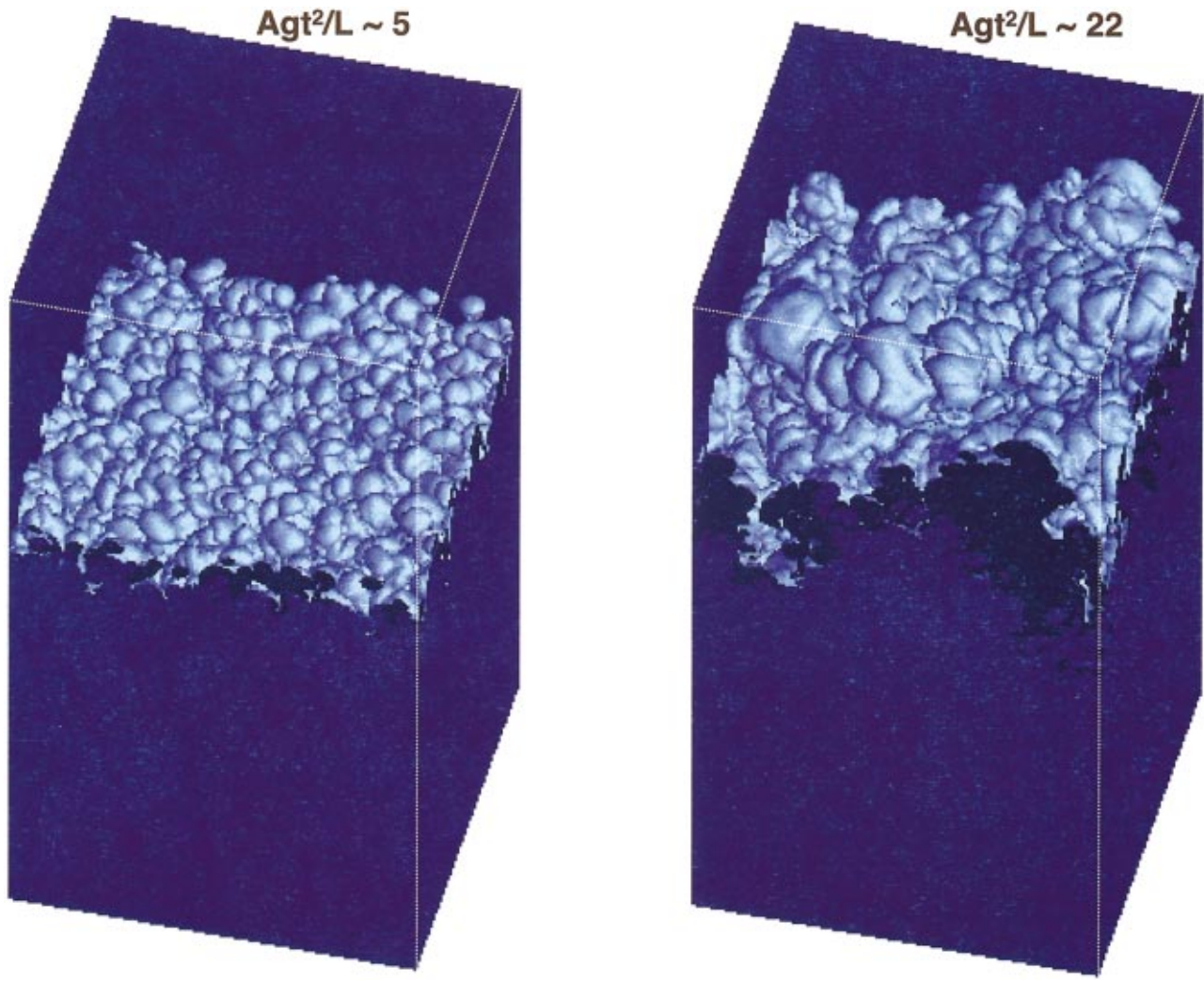


FIG. 6. (Color) Isosurfaces from TURMOIL3D where “heavy” fluid concentration=0.99.

15 December 2024 19:26:09

In most experiments and all with the LEM, the fluids were immiscible and the fastest growing wave was determined by surface tension,³ namely,

$$k_p \sim \sqrt{\delta \rho g / 3\sigma} \quad (17)$$

and

$$\Gamma(k_p) \sim 0.82 \sqrt{A k_p g}. \quad (18)$$

For the typical set of LEM parameters, $A \sim 1/3$, $g \sim 50g_0$, $\sigma \sim 4$ dyn/cm², the initial dominant mode has $\lambda_p \sim 1$ mm, and $\Gamma \sim 800$ s⁻¹. Since we expect the initial spectrum in the experiments to be broad and continuous, the most unstable mode will dominate initially so that $\lambda_0 = \lambda_p$. Thus, the self-similar evolution can occur over a dynamic range of $L/\lambda_0 \sim 40$ for M256 and 20 for M128, whereas experiments have a broader range $L/\lambda_0 \sim 73$.

Normalizing to these scales helps to clarify the evolution in Figs. 8–10 in which the amplitudes grow rapidly initially and then asymptote to a smaller α_b . The transition is related to the saturation of the imposed initial amplitudes and this launches the mode-coupling phase. The transition occurs near $h_b/L \sim 0.15$ or $Agt^2/L \sim 2$ for M256 and $h_b/L \sim 0.3$ or $Agt^2/L \sim 4$ for M128. This distinction is normalized out by

scaling to λ_0 because the transition begins near $h_b/\lambda_0 \sim 4$ or $Agt^2/\lambda_0 \sim 50$ in both cases. For example, at $Agt^2/\lambda_0 \sim 50$, the imposed modes would have been amplified by $\cosh(\Gamma t) \sim 10^5$ [using Eq. (16)] to $h_b \sim 1-2$ cm. This means that they would be nonlinear since $h_b \sim 4\lambda_0$ and this is consistent with the aspect ratio of the dominant bubbles $D_b/h_b \sim 1/3$ observed in Sec. V. Thus, for our annular initial spectra, the transition in growth rate seems to begin when the first dominant bubble has $\lambda_b \sim \lambda_0$ (mode 32 for M256 and 16 for M128) at about $Agt^2/\lambda_0 \sim 50$. α_b then decreases because the growth mechanism changes from the amplification of the imposed modes to the mode-coupling process (Table III). The experiments do not exhibit such a strong transition and grow faster than the NS possibly because they have a broad initial spectrum and the amplification process extends throughout.

To confirm that the differences between the M128 and M256 cases are due to the initial mode structure rather than the zoning, Youngs performed an additional 256×256×512 simulation initiated with modes 16–32 similar to M128. The result, indicated by the solid line in Fig. 11, reproduces Youngs’ M128 and M256 (dotted and dashed lines). We thus conclude that the evolution of the mixing zone is more sen-

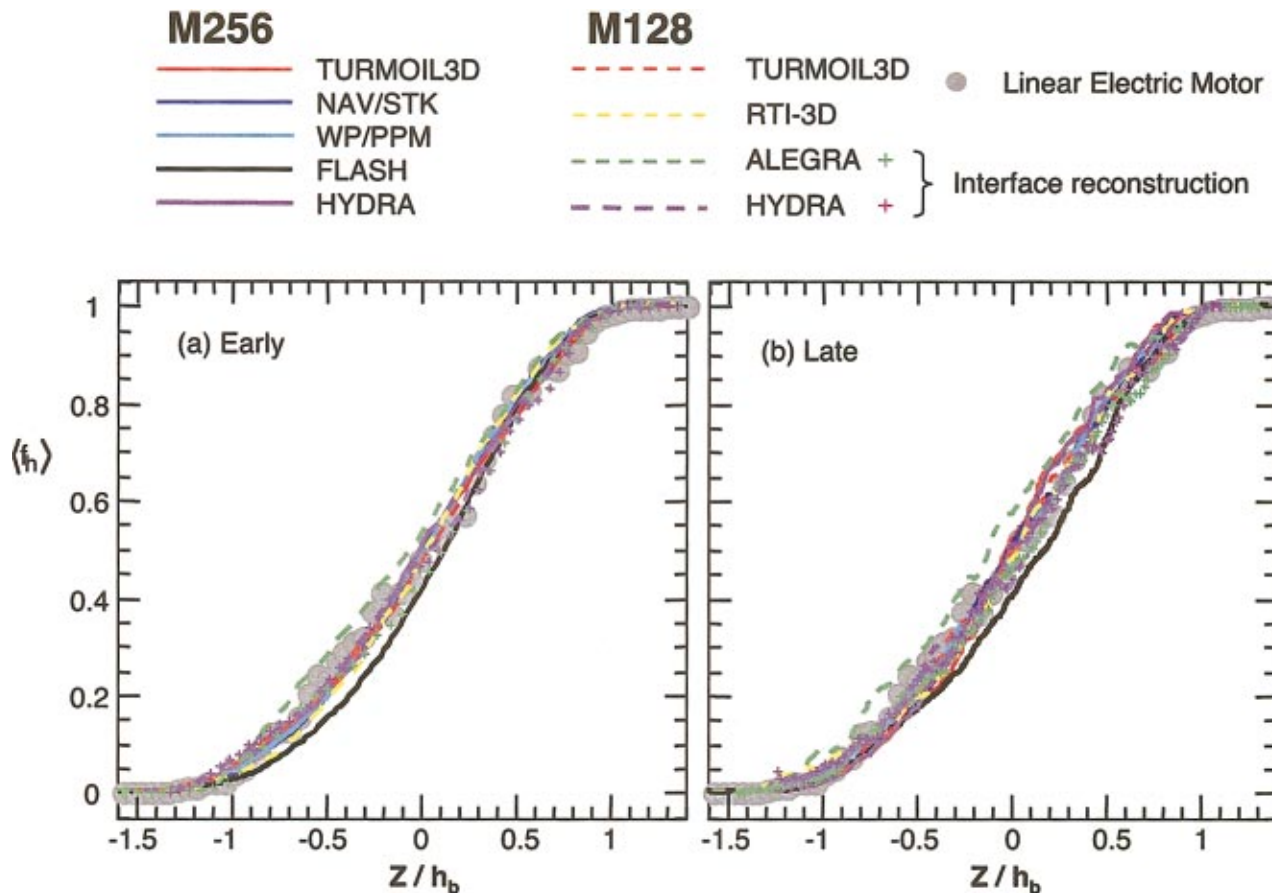


FIG. 7. (Color) Vertical profiles of “heavy” fluid volume fraction averaged over horizontal planes. (a) Early profiles at $Agt^2/L \sim 3$ for ALEGRA and ~ 5 for all other NS. (b) Late profiles at $Agt^2/L \sim 14$ for ALEGRA and ~ 22 for all other NS. Lines are from NS and points are from LEM experiments.

15 December 2024 19:26:09

sitive to the initial perturbation spectrum than the zoning. Of course, the fine scale features and dissipation scale will depend on zoning, but these are much smaller than the inertial scales that determine α_b asymptotically.

D. Analysis for α_b

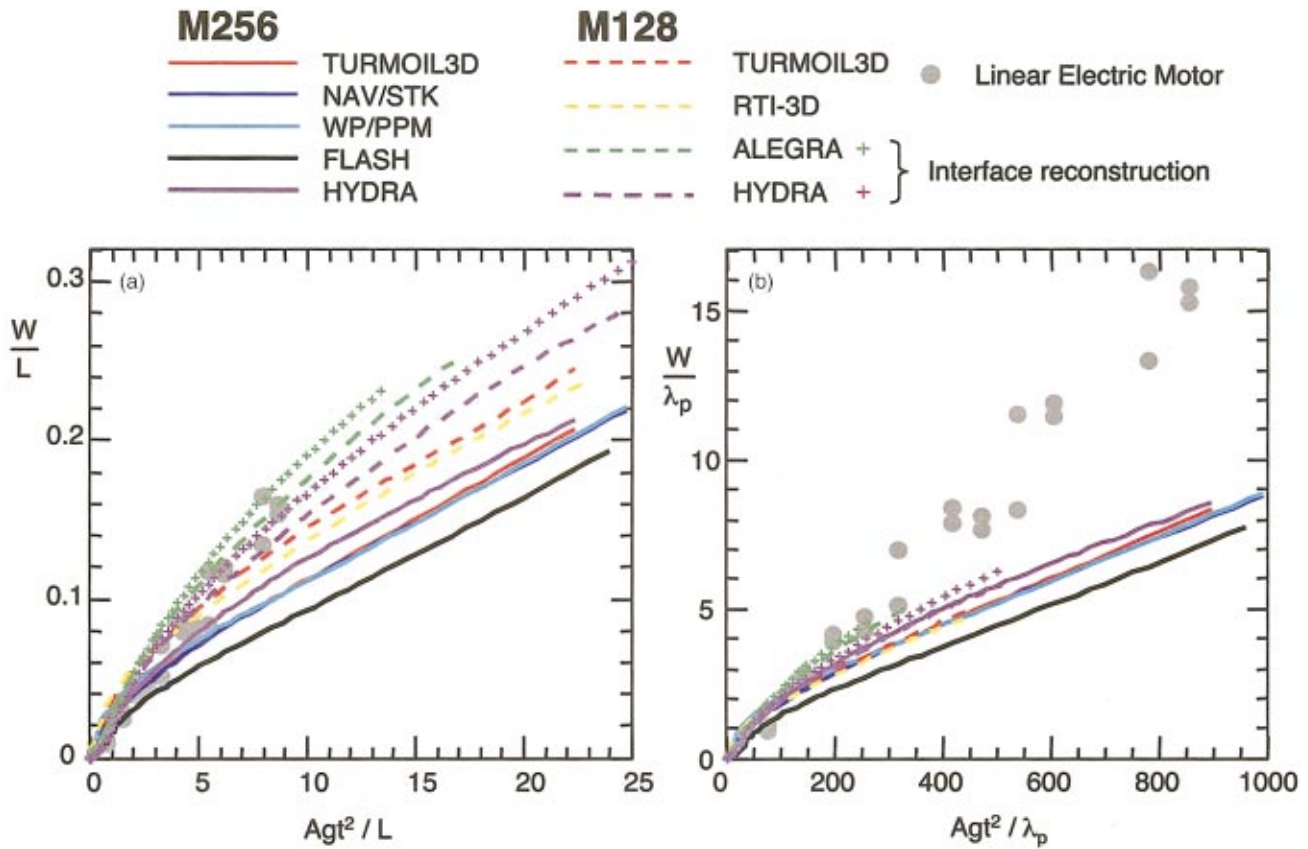
The bubble acceleration constant α_b is obtained here by differentiating h_b with respect to Agt^2 and the result is shown in Fig. 12. The evolution of α_b exhibits the transition between the amplification of the imposed modes and the mode-coupling phase. This occurs near $Agt^2/\lambda_0 \sim 50-100$ when all of the imposed modes in our annular spectrum have saturated. Then, α_b decays from a peak value of ≤ 0.1 as the saturated modes couple nonlinearly to longer wavelengths. As seen in Figs. 8–11, the steady state value of $\alpha_b \sim 0.025$ is obtained at different values of $Agt^2/L \sim 6$ and 12 for M256 and M128 but at the same value of near $Agt^2/\lambda_0 \sim 250$ for both.

The asymptotic values of α_b are summarized and compared with published experiments in Fig. 13. The values ascribed to the NS are averaged over $Agt^2 > 200\lambda_0$ and the reported experimental values are shown in histogram form. The sample average and variance are $\alpha_b \sim 0.025 \pm 0.003$ for the NS and $\alpha_b \sim 0.057 \pm 0.008$ for the experiments. This difference is consistent with the historical record in Fig. 1. It should be emphasized that the value of α_b from these NS

should be regarded as a lower bound due to mode coupling since long wavelength modes are not imposed explicitly. As such, this low value is insensitive to the initial conditions because it is due to the nonlinear coupling of saturated high- k modes. If the initial spectrum has significant long wavelength components, they will grow exponentially and increase α_b , as shown explicitly by Linden, Redondo, and Youngs.⁴⁰ Further NS with broadband initial perturbations are required to clarify these issues.

V. SELF-SIMILAR BUBBLE DYNAMICS

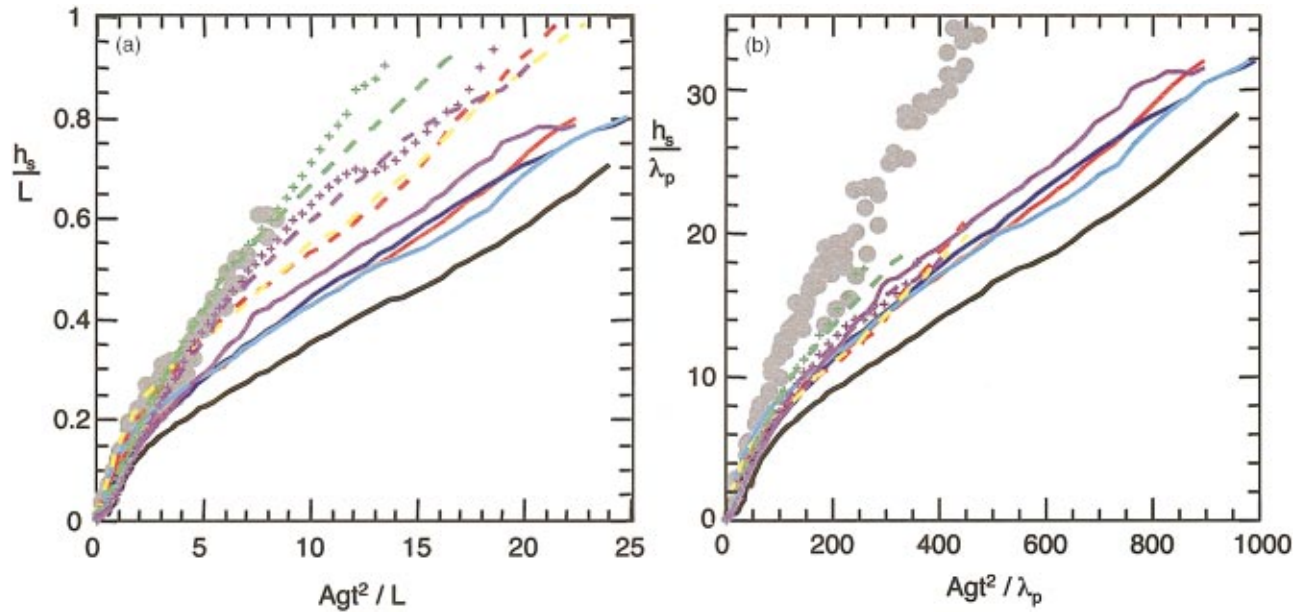
In lieu of a theory for α_b to elucidate the discrepancy between NS and experiments, it is helpful to construct models for α_b based on well known bubble dynamics.^{14,17,20–22,32,44,45,48,49} Such models postulate that the dominant bubbles have the single bubble velocity given by Eq. (2) with a diameter that grows self-similarly $D_b \propto h_b$. This is tested in this section by analyzing output data from the NS. The diameter is computed from the autocorrelation function of the bubble front. However, it is found necessary to characterize the entrainment or diffusion of heavy fluid into the bubble because it reduces the density difference in Eq. (2) between the bubble and the upstream (heavy) fluid to $\delta\rho < \rho_h - \rho_l$. Entrainment is expected from the vortical motion induced by the velocity shear at the bubble boundaries

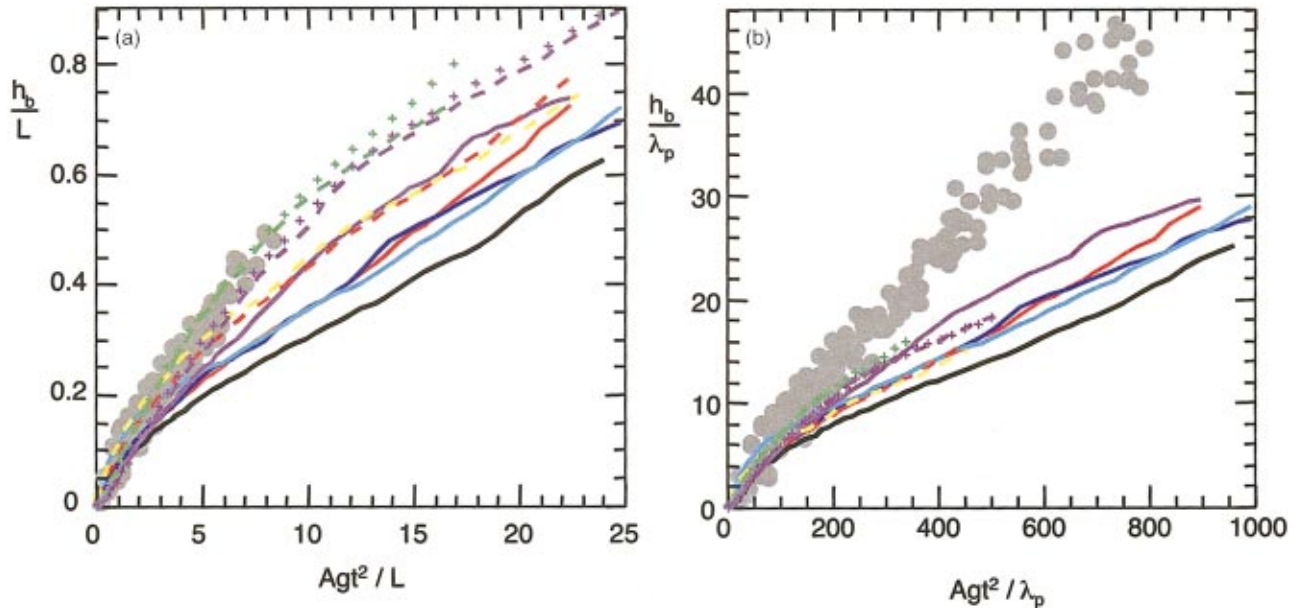
FIG. 8. (Color) Evolution of integral mixing width W scaled to (a) box width L and (b) dominant initial mode λ_p .

but it may be exacerbated in these NS because they are initiated with small scales that are marginally resolved. This section describes the analysis of the NS data for D_b/h_b and $\delta\rho$ within the context of bubble dynamics (Fig. 14).

A. Bubble diameter

The diameter of the dominant bubbles D_b is obtained by performing a correlation analysis of the bubble front

FIG. 9. (Color) Evolution of spike amplitude h_s scaled to (a) box width L and (b) dominant initial mode λ_p .

FIG. 10. (Color) Evolution of bubble amplitude h_b scaled to (a) box width L and (b) dominant initial mode λ_p .

$Z_b(x,y)$, which we define as the 2D isosurface where $f_h = 0.99$. Two representations of Z_b from TURMOIL3D are shown in Fig. 15 for $Agt^2/L=5$ and 22. The top row shows shaded surface plots for $Z_b > 0.75h_b$ so that the leading bubbles appear light. The bottom row shows the corresponding 2D images in a more quantitative format with the height indicated in the look-up table. The vertical domain is collapsed to enhance the contrast: the dominant bubbles with $Z_b \geq h_b$ appear black and the region at $Z_b < 0.75h_b$ appears white. There are more than 20 dominant bubbles near $Agt^2/L=5$ that coalesce to three larger bubbles by $Agt^2/L=22$. All of the NS exhibit this self-similar growth as shown in Figs. 16 and 17 for bubbles (Z_b) and Figs. 18 and 19 for spikes (Z_s). The relative size of the bubbles and spikes are similar in these NS except in the two PPM codes WP/PPM and FLASH which exhibit relatively smaller diameters. This cannot be attributed to viscosity since the WP/PPM has a smaller $\varpi \sim 0.28$ than NAV/STK ($\varpi \sim 0.53$) but it has a larger D_b . We also observe that the dominant bubbles and spikes are dis-

tributed throughout the cross section in most NS except ALEGRA which has bubbles near the edges early in time.

The diameter of the dominant bubbles D_b is obtained from the correlation function

$$\zeta_b(x,y) = \frac{\sum (Z_b(x',y') - \langle Z_b \rangle)(Z_b(x'+x,y'+y) - \langle Z_b \rangle)}{\sum (Z_b(x',y') - \langle Z_b \rangle)^2} \quad (19)$$

of the bubble front $Z_b(x,y)$, where the summations are performed over $0 \leq x', y' \leq L$. Representative images of ζ_b are shown in Fig. 20 with the origin $(x,y=0)$ in the center. The top two images are from TURMOIL3D at $Agt^2/L=5$ and 22 and the lower images are from ALEGRA with IR at Agt^2/L

TABLE III. Alphas and self-similarity. For $Agt^2/L \geq 10$.

Simulation	Alpha		Diameter/Amplitude	
	Bubble	Spike	Bubble	Spike
256×256×512				
TURMOIL3D	0.028	0.030	0.37	0.32
FLASH	0.022	0.027	0.44	0.38
NAV/STK	0.022	0.024	0.33	0.34
WP/PPM	0.024	0.026	0.43	0.31
HYDRA	0.029	0.027	0.34	0.27
128×128×256				
TURMOIL3D	0.027	0.042	0.35	0.30
RTI-3D	0.023	0.036	0.47	0.28
ALEGRA	0.024	0.038	0.29	0.23
ALEGRA_IR	0.030	0.054	0.24	0.19
HYDRA	0.024	0.030	0.26	0.17
HYDRA_IR	0.024	0.032	0.23	0.27

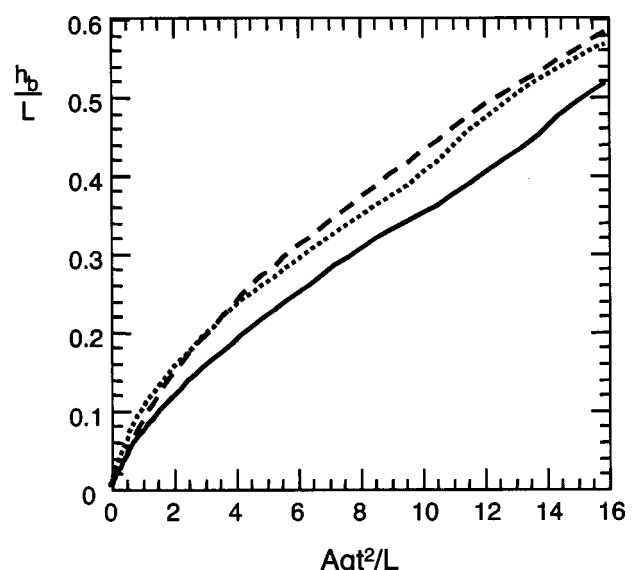
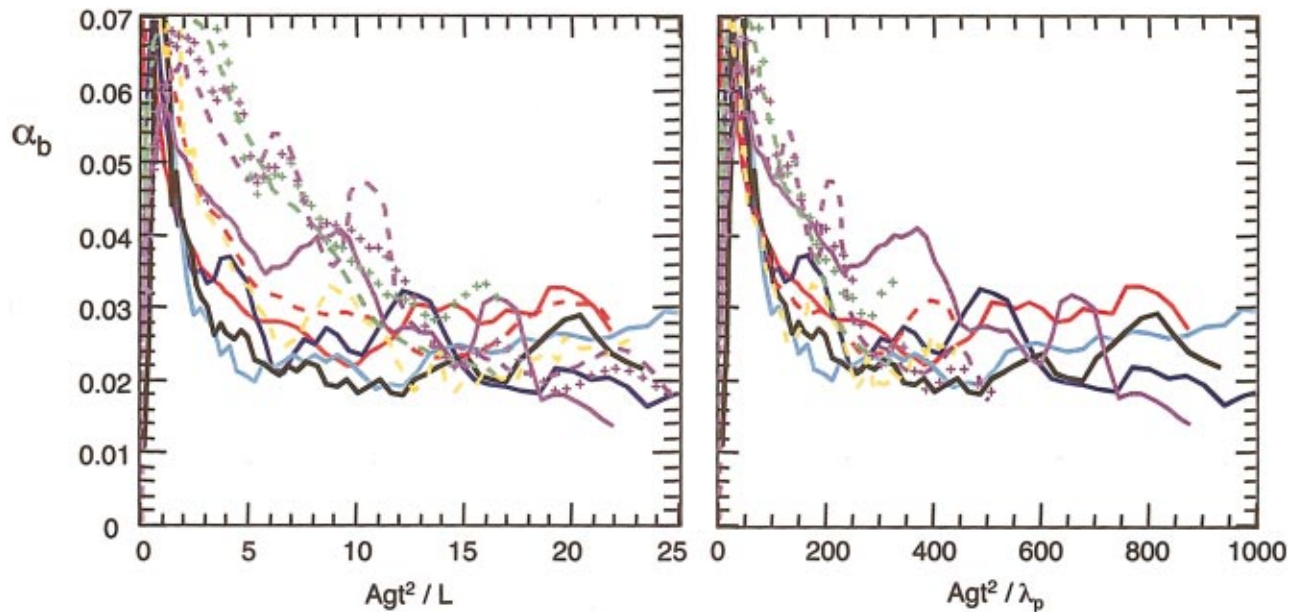


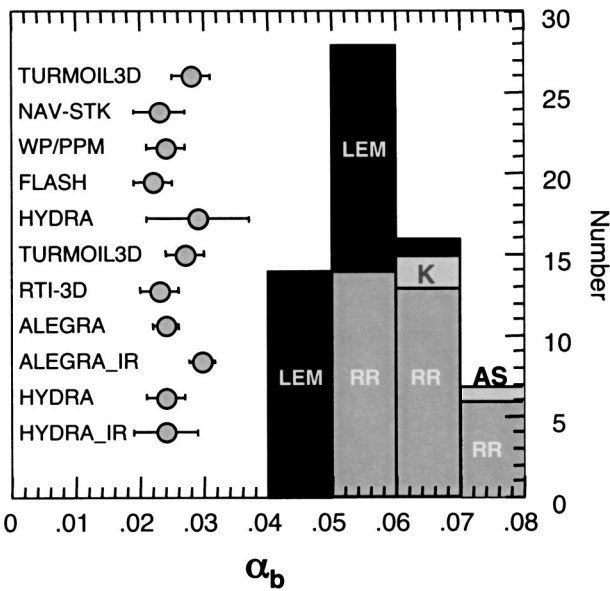
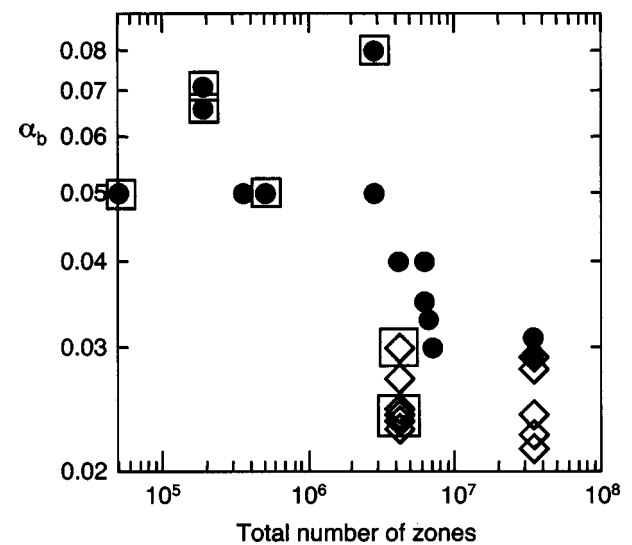
FIG. 11. Evolution of bubble amplitude from TURMOIL3D for M256 (solid), M128 (dashed) and a 256×256×512 zone simulation with initial perturbations similar to M128 (dotted).

FIG. 12. (Color) Evolution of α_b obtained by differentiating h_b with respect to Agt^2 .

=3 and 14. The look-up-table has been modified so that white corresponds to where $\zeta_b=1$ at the origin and $\zeta_b=0.3$ for the contour corresponding to the bubble radius as discussed below. The bottom row shows the radial profiles of the azimuthally averaged correlation function $\langle \zeta_b \rangle_\theta$ for all of the NS (except HYDRA) with our standard color coding. ζ_b decreases from unity with the radial displacement at a rate characteristic of the relative size and location of the dominant bubbles. If the bubbles are distributed randomly, ζ_b asymptotes to a very small value, as indicated for both ALEGRA images and for TURMOIL3D at $Agt^2/L=5$. For TURMOIL3D at $Agt^2/L=22$, there are three dominant bubbles that are

closely aligned near 45° in Fig. 20 and this produces the oscillatory ridge in ζ_b at 45° with a second peak $\zeta_b=0.38$. This oscillation is significantly smaller in the azimuthal average so that $\langle \zeta_b \rangle_\theta$ remains moderately well behaved.

The technique for extracting D_b from $\langle \zeta_b \rangle_\theta$ was developed by analyzing test images with various round bubbles of known sizes. It is found that the bubble radius corresponds to the radial displacement where $\langle \zeta_b \rangle_\theta=0.3$. This value depends slightly on the relative number and size of the bubbles because they determine $\langle Z_b \rangle$ in Eq. (19), but the uncertainty is $<\pm 15\%$ for our conditions. Another uncertainty is associated with the asymmetry in the $\zeta_b=0.3$ contour (white) seen in TURMOIL3D at $Agt^2/L=22$, which has a radius of 2.3 cm at 45° and 1.3 cm at -45° . Since the elongation is due to the

FIG. 13. Comparison of α_b from NS (points) and experiments in histogram form. LEM is from Linear Electric Motor (Ref. 30), RR from “rocket rig” (Ref. 24), K from Kucherenko *et al.* (Ref. 27), AS is from Andrews and Spalding (Ref. 26).FIG. 14. Comparison of α_b with other 3D simulations. Diamonds represent current NS and circles represent previous NS. Those enclosed in boxes used interface reconstruction or tracking.

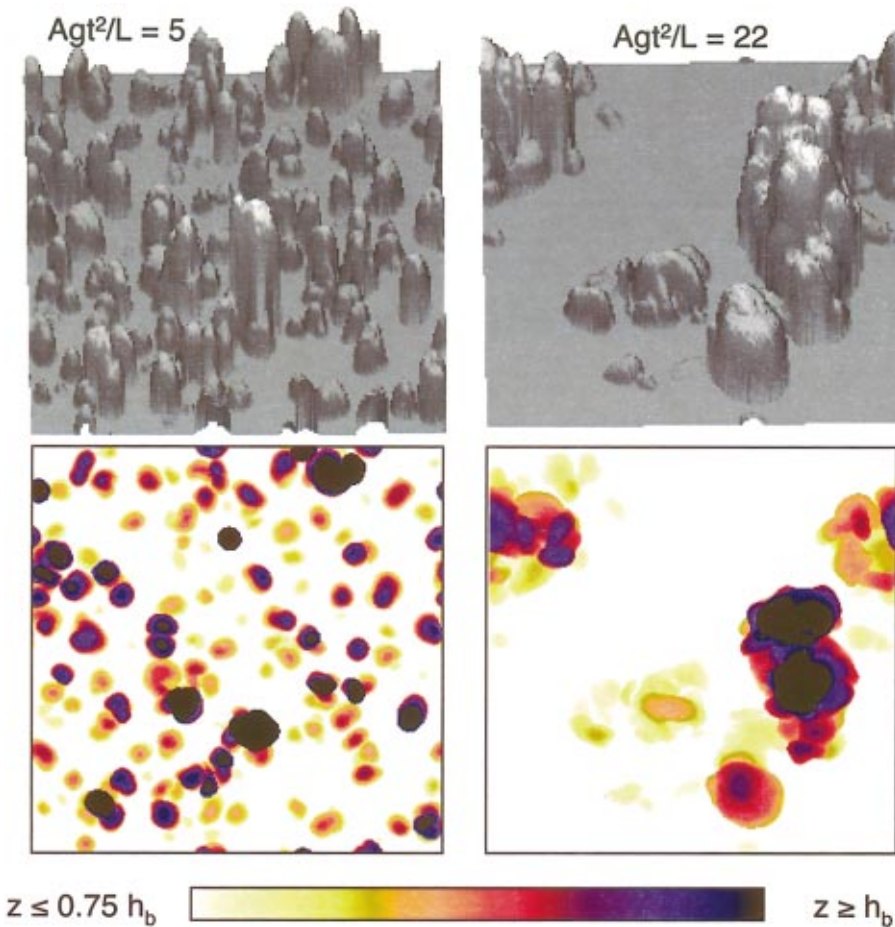


FIG. 15. (Color) Bubble fronts in the region $Z_b(x,y) \sim 0.75 - 1 h_b$ from TURMOIL3D. Top row shows shaded surface plots. Bottom row shows corresponding false color images with look-up table.

satellite peak in ζ_b , the azimuthal average radius of 1.5 cm is 15% larger than the intrinsic bubble radius (from -45° profile). We compensate for the asymmetry in this case by choosing the 1.3 cm radius, but it is not necessary for the other cases since the eccentricity is < 1.1 . To summarize, the bubble radius is taken to be the radial displacement where $\langle \zeta_b \rangle_\theta = 0.3$ and the combined error is estimated to be $\sim \pm 20\%$.

The values of D_b/h_b from the NS (diamonds) are compared with each other and LEM experiments³⁰ (circles) in Fig. 21. As with α_b , only the late time values are used so that it is less sensitive to the initial conditions. The NS give $D_b/h_b \sim 0.38 \pm 25\%$ and $D_s/h_s \sim 0.31 \pm 25\%$ compared to $0.4 \pm 10\%$ and $0.2 \pm 10\%$ from the LEM. Using Daly's suggestion Eq. (8), these results would correspond to $\lambda_b/h_b \sim 0.51 \pm 25\%$ from the NS in good agreement with $0.54 \pm 15\%$ from the LEM.

B. Entrainment and diffusion

The entrainment or diffusion of heavy fluid into the bubbles is also important because they increase the effective bubble density to $\rho_b > \rho_l$ and this reduces their buoyancy and thus their velocity $\propto \sqrt{(\rho_h - \rho_b)g D_b}$. There are two plausible mechanisms for entrainment involving (1) the vortices generated at the bubble boundaries due to the velocity shear and (2) mode coupling. The vortical motion folds heavy fluid into the bubbles with short scale spirals that become either en-

trained or atomically mixed in the NS with and without IR, respectively. Mode coupling can also enhance diffusion because the daughter products are both at shorter and longer wavelengths ($k \pm \delta k$) than the parent modes. The $k + \delta k$ mode is poorly resolved in these NS because it has only a few zones/wavelength and this exacerbates the numerical diffusion. Unfortunately, the NS never recover from this diffusion because subsequent generations of bubbles are comprised of mixed fluid. The density increase can be characterized in two related ways, namely, by directly calculating the density in the bubbles near the front or indirectly from the atomic mixing parameter θ .

The densification of bubbles is seen directly in the sample vertical density slices in Fig. 22 from each NS late in time. The bubbles appear gray rather than black (except with IR) and this signifies that they have intermediate densities $\rho_l < \rho_b < \rho_h$ as indicated by the look-up table. Sample vertical density profiles through the dominant bubbles are shown in Fig. 23 at the location of the dotted lines in Fig. 22. The densities are in the range of $2 - 2.5 \text{ g/cm}^3$ without IR, whereas ρ_b toggles between ρ_l and ρ_h with IR. To obtain ρ_b consistently with and without IR, we compute averages for the leading bubbles within a radius $D_b/2$ of the highest bubble tip. This is exemplified for vertical slices of density and vertical velocity in Fig. 24 from TURMOIL3D without IR at $Agt^2/L = 22$ and with IR from ALEGRA at $Agt^2/L = 14$. The averages are computed for the region between the bubble

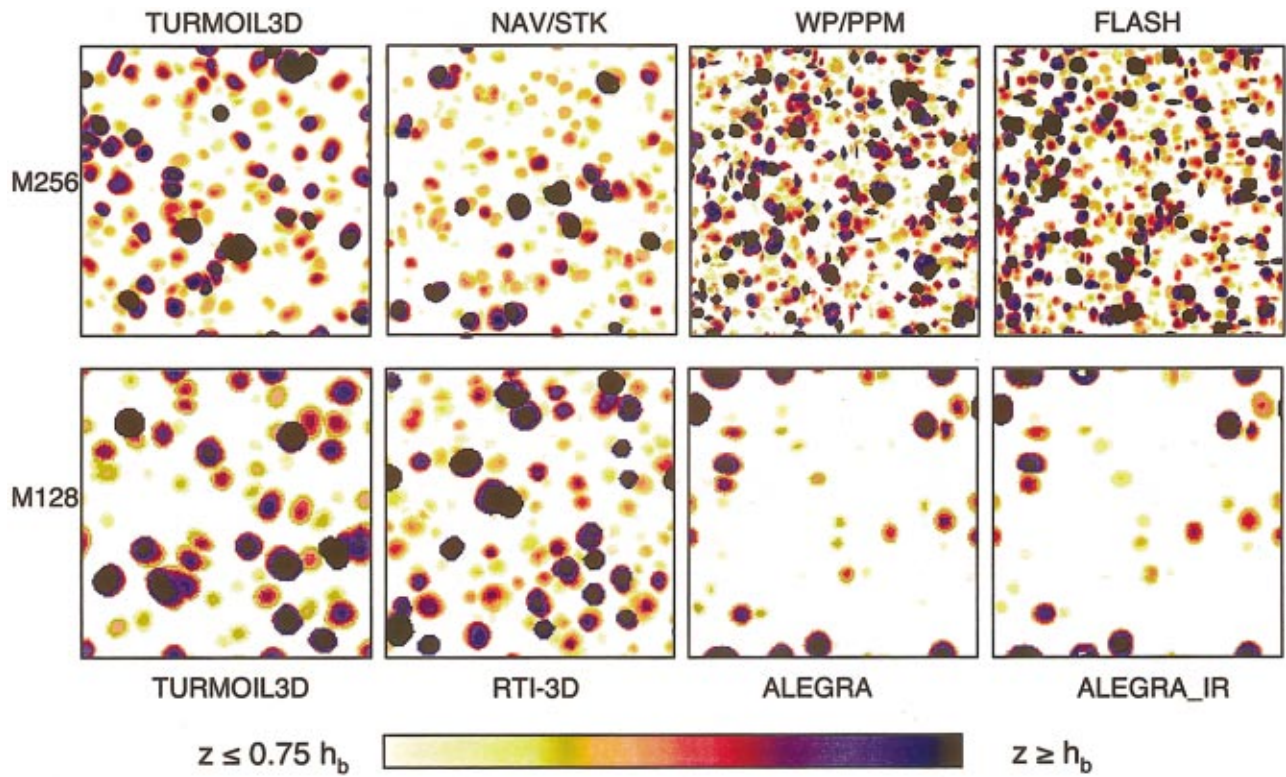


FIG. 16. (Color) Early false color images of BUBBLE FRONTS with look-up table representing $Z_b \sim 0.75 - 1 h_b$. Time corresponds to $Agt^2/L \sim 3$ for ALEGRA and ~ 5 for all other NS.

front $Z_b(x,y)$ (solid line) and the maximum $(Z_b) - D_b/2$ (dashed line) in the vertical slices (top row). For example, there are 1.5×10^5 zones in the bubble samples with an average $\rho_b = 2.35 \text{ g/cm}^{-3}$ and $V_b = 0.7 \text{ cm/s}$ for TURMOIL3D at

$Agt^2/L = 22$ and there are 5800 sample zones with $\rho_b = 2.0 \text{ g/cm}^{-3}$ and $V_b = 0.71 \text{ cm/s}$ for ALEGRA at $Agt^2/L = 14$. The corresponding values for all NS are summarized in Table IV. The bottom row in Fig. 23 shows horizontal slices

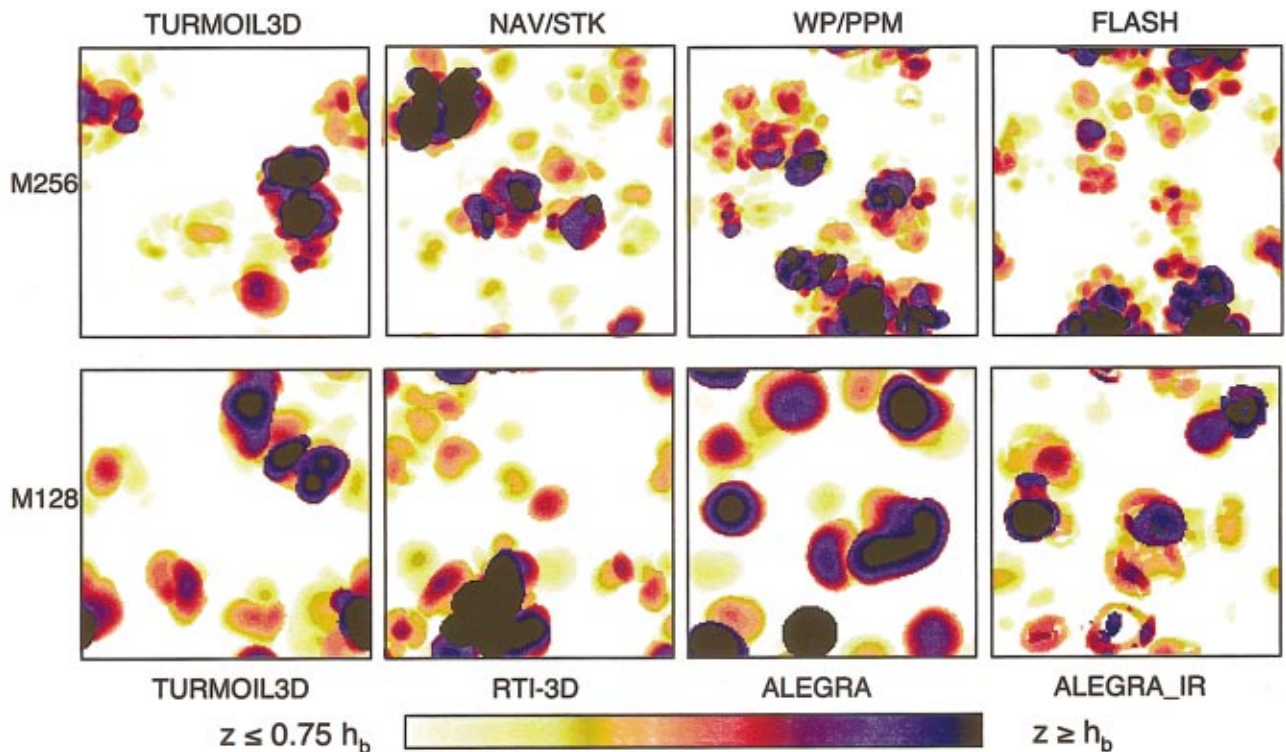


FIG. 17. (Color) Late false color images of BUBBLE FRONTS with look-up table representing $Z_b \sim 0.75 - 1 h_b$. Time corresponds to $Agt^2/L \sim 14$ for ALEGRA and ~ 22 for all other NS.

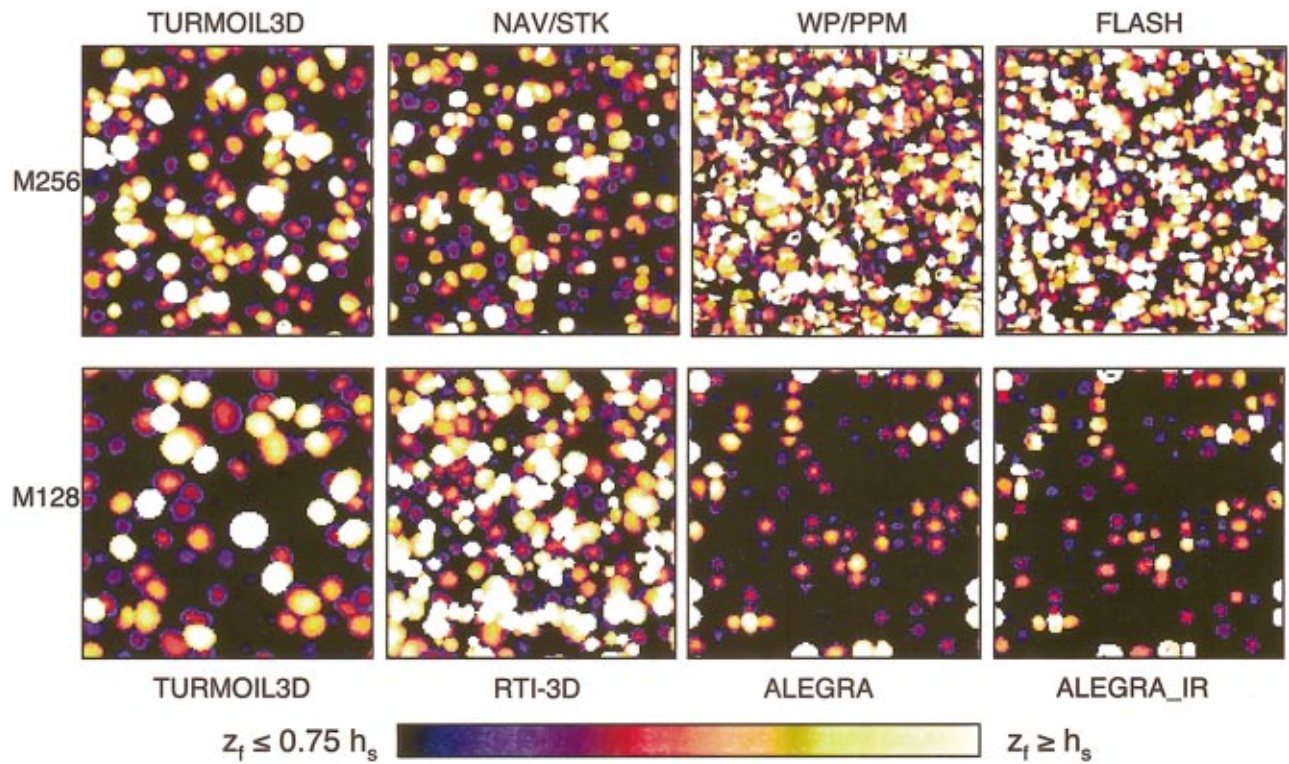


FIG. 18. (Color) Early false color images of SPIKE FRONTS with look-up table representing $Z_s \sim 0.75 - 1 h_b$. Time corresponds to $Agt^2/L \sim 3$ for ALEGRA and ~ 5 for all other NS.

at the height of the dashed lines in the top row. The dashed lines in the bottom row indicate the location of the vertical slices on top. For TURMOIL3D, the diffusion of heavy fluid into the bubbles is evident because the bubbles are lighter

than black ($\rho_b > 1 \text{ g/cm}^{-3}$). For ALEGRA with IR, the diffusion is limited to the interfacial zones, but the entrainment can be seen by comparing the density and velocity images. The density images show bubbles with light fluid (black)

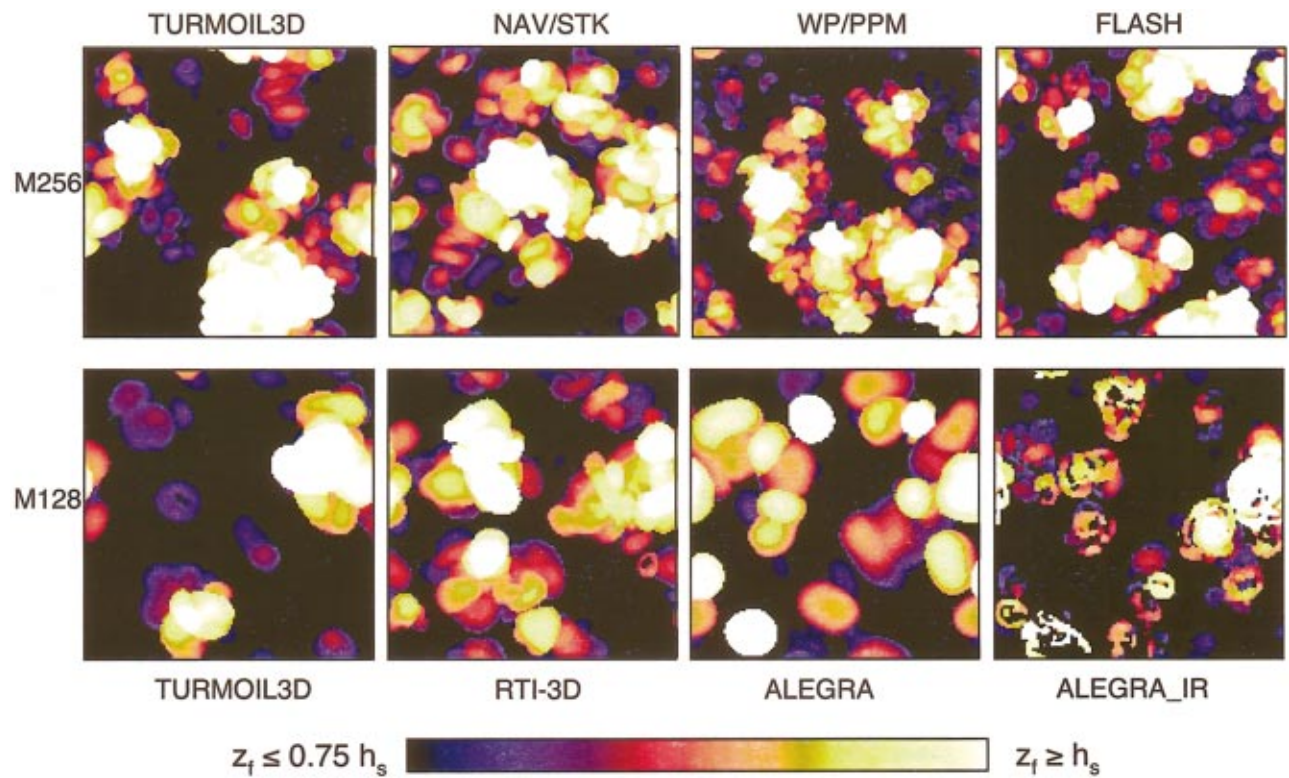


FIG. 19. (Color) Late false color images of SPIKE FRONTS with look-up table representing $Z_s \sim 0.75 - 1 h_b$. Time corresponds to $Agt^2/L \sim 14$ for ALEGRA and ~ 22 for all other NS.

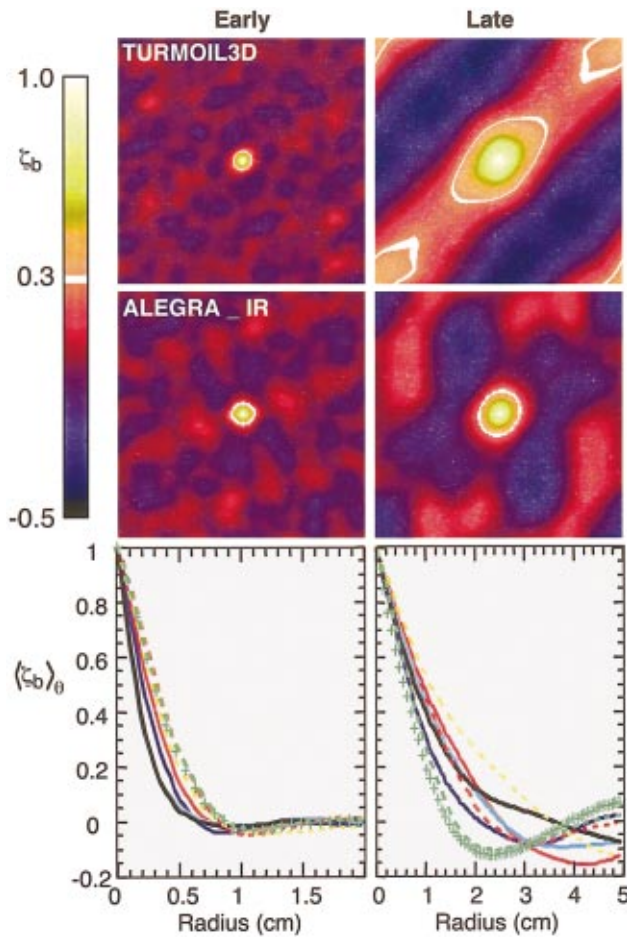


FIG. 20. (Color) Correlation images from TURMOIL3D (top row) and ALEGRA with IR (middle row) and average profiles for all NS.

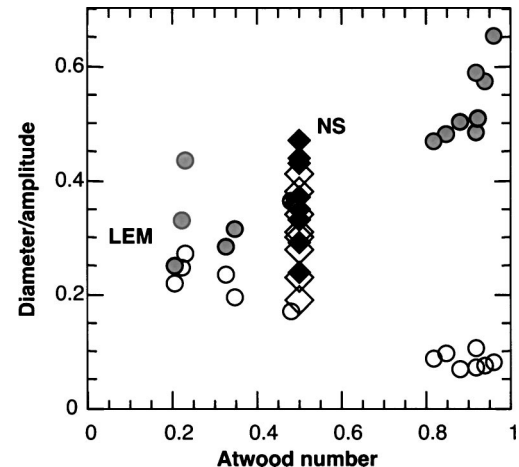


FIG. 21. Aspect ratio (diameter/amplitude) of bubbles (solid) and spikes (open) from LEM experiments (circles) and the present NS (diamonds).

surrounding heavy fluid (white) but the velocity images show a light central core indicating that both fluids within the bubbles are co-moving. This can also be seen in Fig. 25 by plotting the density vs velocity in zones within the averaging region. Without IR, TURMOIL3D exhibits densities $>1.7 \text{ g/cm}^3$. With IR, ALEGRA shows a bimodal density distribution with 21% pure light fluid and 30% pure heavy fluid, both of which have similar velocities. This is a clear indication that the heavy fluid is entrained with the light fluid in the bubbles. The remaining 49% of the zones have intermediate densities due to numerical smearing in the interfacial zones.

The degree of interfluid mixing can also be characterized by the molecular mixing profile

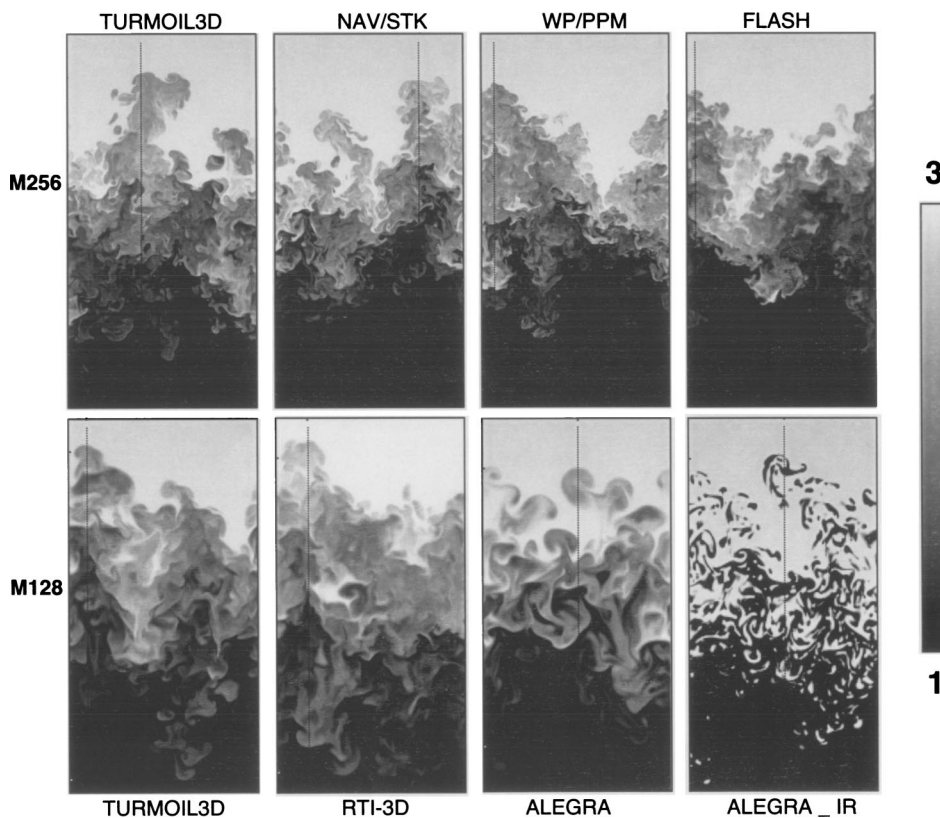


FIG. 22. 2D density slices showing dominant bubbles at $Agt^2/L \sim 14$ for ALEGRA and ~ 22 for all other NS. Dotted lines indicate location of density profiles in Fig. 23.

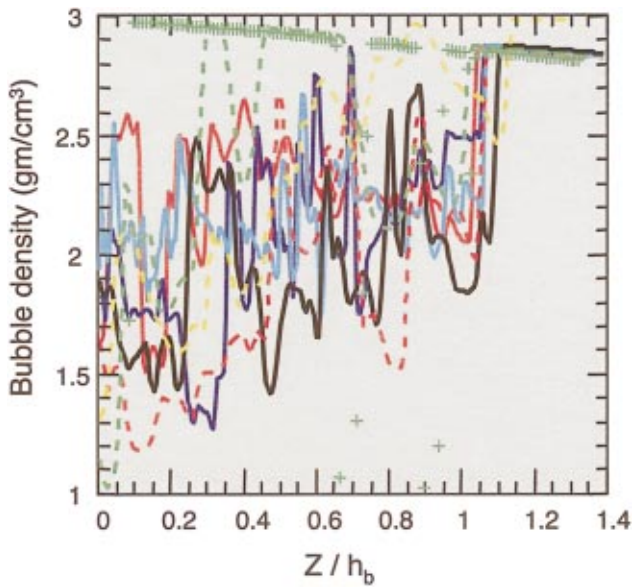


FIG. 23. (Color) Density profiles through dominant bubbles indicated by dotted lines in Fig. 22.

TABLE IV. Effective bubble density, global molecular mixing parameter, and multimode Froude-type number Fr.

Simulation	ρ_b	Θ	Fr
256×256×512			
TURMOIL3D	2.35	0.79	1.00
FLASH	2.46	0.80	0.89
NAV/STK	2.56	0.80	1.04
WP/PPM	2.43	0.79	0.91
HYDRA	2.42	0.80	0.95
128×128×256			
TURMOIL3D	2.38	0.80	1.01
RTI-3D	2.72	0.84	0.92
ALEGRA	2.51	0.77	0.92
ALEGRA_IR	1.98	0.28	0.93
HYDRA	2.40	0.78	0.94
HYDRA_IR	2.09	0.27	0.84

$$\theta(z) = \frac{\langle f_h f_l \rangle}{\langle f_h \rangle \langle f_l \rangle}. \quad (20)$$

$\theta=0$ signifies no mixing such as at $t=0$ and $\theta=1$ indicates complete molecular mixing. Late time profiles of θ are exemplified in Fig. 26 for all NS with our standard color cod-

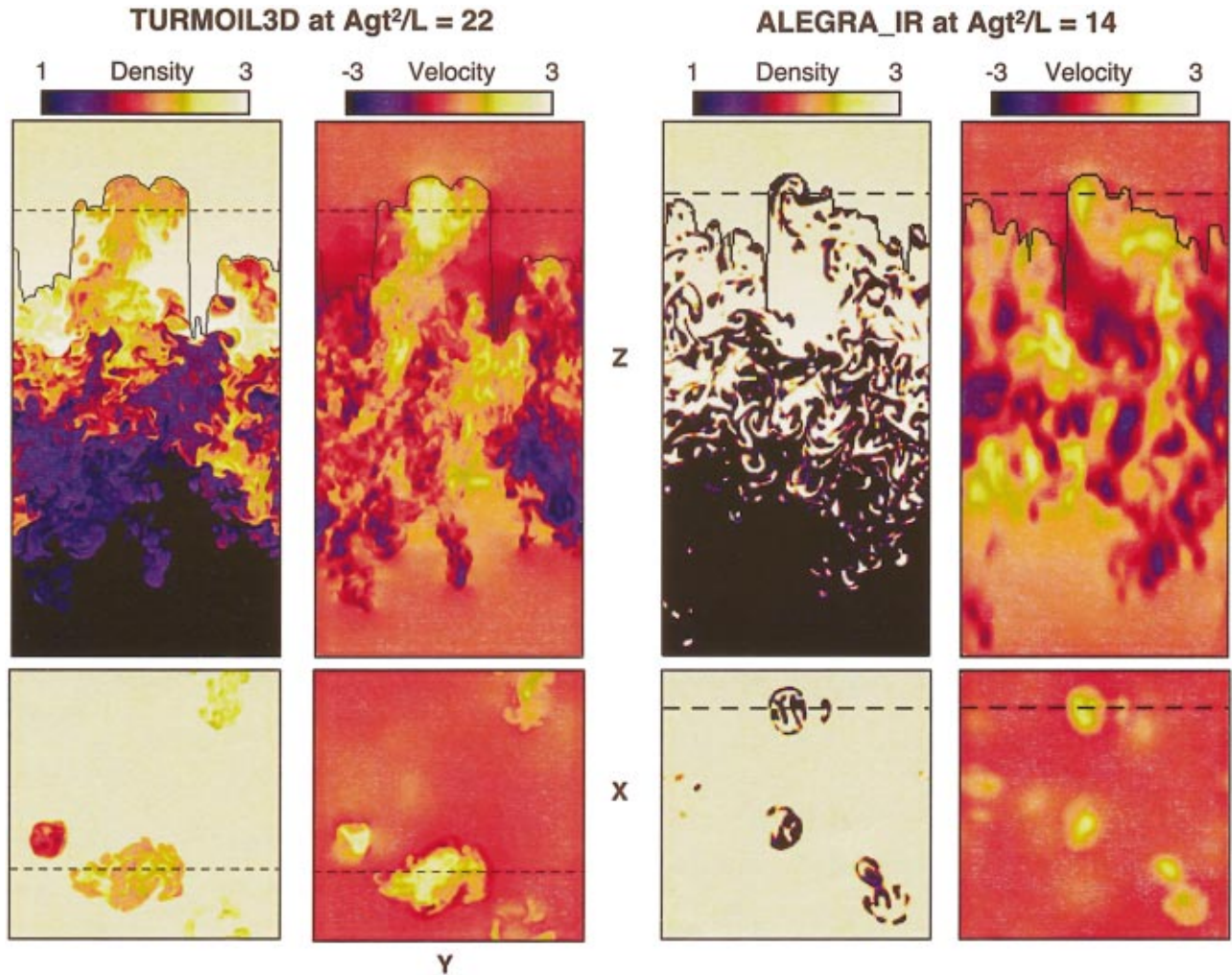


FIG. 24. (Color) Vertical and horizontal slices of density and vertical velocity in cgs units at $Agt^2/L \sim 22$ for TURMOIL3D and at ~ 14 for ALEGRA with IR. Dashed lines indicate position of complementary images.

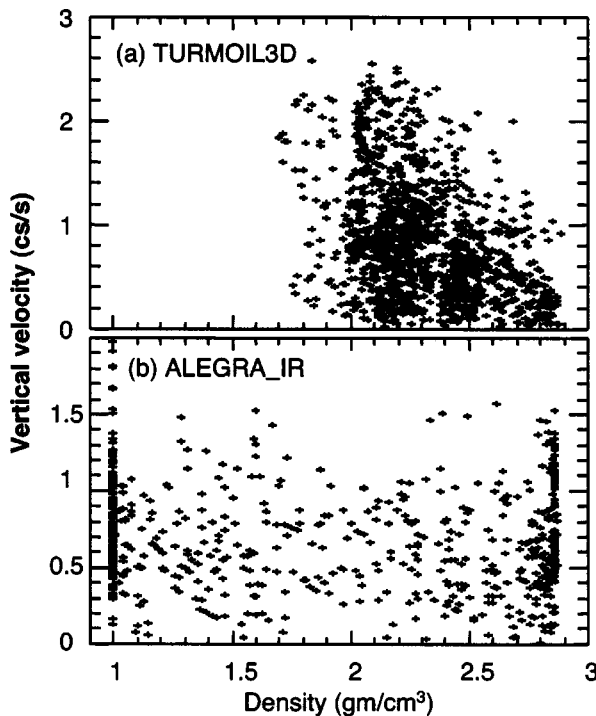


FIG. 25. Point by point distribution of vertical velocity vs density from (a) TURMOIL3D and (b) ALEGRA with IR from Fig. 24. TURMOIL3D has no points with pure fluid and ALEGRA has 51% of the points with pure fluid (21% with density $<1.05 \text{ g/cm}^3$ and 30% have $>2.7 \text{ g/cm}^3$) even with IR.

ing. The NS without IR have similar values $\Theta \sim 0.8$ and ALEGRA and HYDRA with IR have $\Theta \sim 0.3$ due to the numerical smearing in the interfacial zones. The spikes ($Z < 0$) exhibit a slightly larger value of θ than bubbles ($Z > 0$) possibly because they are narrower than bubbles (Fig. 20) and the diffusion scale represents a larger fraction of their size. It is also useful to define the global molecular mixing parameter as

$$\Theta \equiv \frac{\int \langle f_h f_l \rangle dz}{\int \langle f_h \rangle \langle f_l \rangle dz} \quad (21)$$

because it is proportional to the total reaction rate if the two fluids are reactive, but it is within 1% of the average value of θ across the mixing zone. The values of $\Theta \sim 0.8$, as summarized in Table IV, are similar to the 0.7 observed by Wilson and Andrews⁷⁷ and calculated in direct NS (DNS) by Cook and Zhou.⁷⁸ The temporal variation of Θ is shown in Fig. 27 for TURMOIL3D NS M256 (solid line) and M128 (dashed line). Points from the other NS are also shown at early and late times. The molecular mixing increases to a steady value of 0.8 at $Agt^2/\lambda_0 \sim 30$ which is near the nonlinear saturation of the imposed modes as discussed in Sec. IV. This is important because the larger bubbles that dominate later in time are constructed of the earlier smaller bubbles which are heavily mixed, and molecular mixing is not reversible. Thus, the larger bubbles also have a smaller density contrast than the initial value and this may contribute to the reduced value of α_b .

The relation between Θ and ρ_b is shown in Fig. 28. The points are from the NS with the open and solid points being

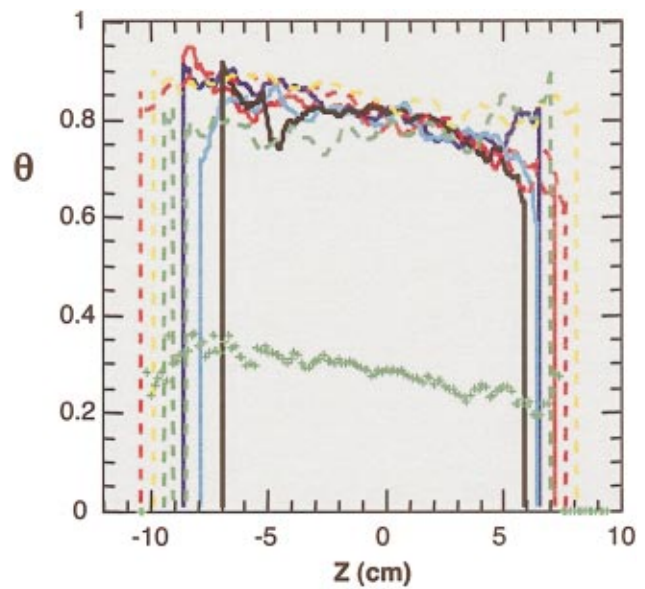


FIG. 26. (Color) Vertical profile of molecular mixing parameter Θ .

at early and late times. For example, $\Theta \sim 0.79$ for TURMOIL3D without IR and this corresponds to $\rho_b \sim 2.35 \text{ g/cm}^3$. With IR, ALEGRA has $\Theta \sim 0.28$ due to the zones at the interface between the pure fluids. Near the midplane, Andrews suggests the following relation:

$$\rho_b \sim \rho_h - (\rho_h - \rho_l) \sqrt{1 - \Theta} \quad (22)$$

which is represented by the line in Fig. 28. The bubble densities from the NS generally exceed Eq. (22), but they both indicate that the bubble density increases with molecular mixing.

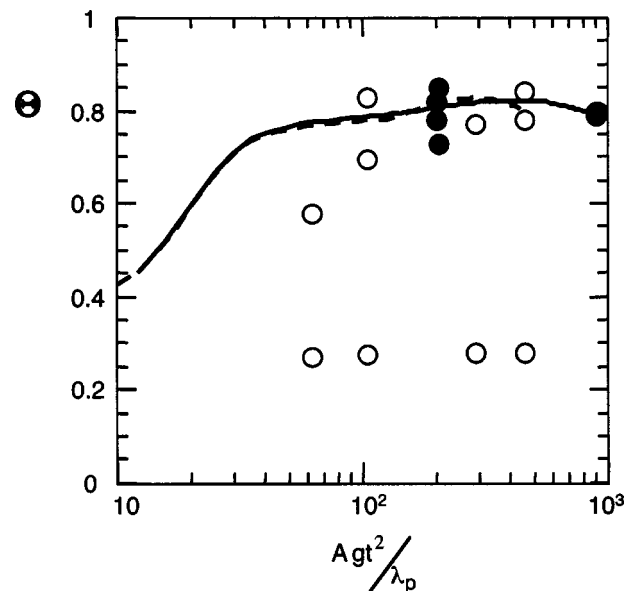


FIG. 27. Evolution of global molecular mixing parameter Θ . Lines from TURMOIL3D for M256 (solid) and M128 (dashed) and points from other NS for M256 (solid) and M128 (dashed).

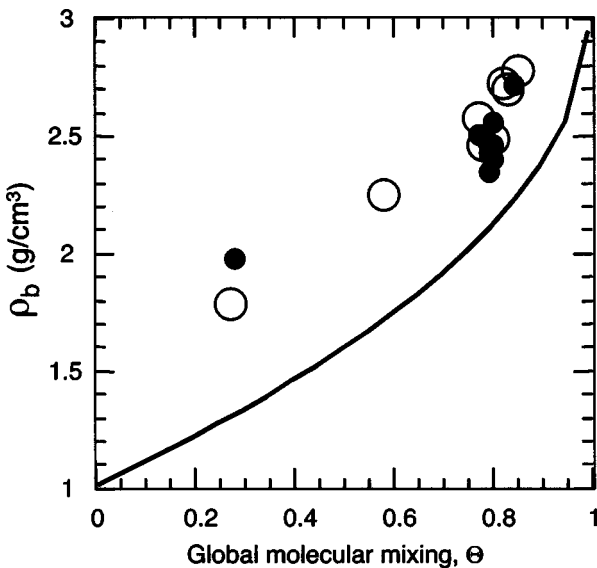


FIG. 28. Density of dominant bubbles ρ_b vs global mixing parameter Θ . Points are NS at early (open) and late (solid) times and line is from Eq. (22).

C. Effective Froude-type number of dominant bubbles

Using our values of D_b and ρ_b , it is possible to infer an effective Froude-type number Fr for the dominant bubbles once their velocity V_b is determined. This is done for the same bubble volume used in calculating ρ_b , namely, the region bounded by the bubble front $Z_b(x,y)$ and the maximum $(Z_b) - D_b/2$ as exemplified in Fig. 24 for a 2D slice. Then, the effective Froude-type number is defined as

$$Fr \equiv \frac{V_b}{\sqrt{(\rho_h - \rho_b)gD_b/2\rho_h}}. \quad (23)$$

In order to assess the effect of entrainment, it is also useful to define a Froude-like number using the initial densities, namely,

$$Fr_0 \equiv \frac{V_b}{\sqrt{(\rho_h - \rho_l)gD_b/2\rho_h}}. \quad (24)$$

Both values are compared with experiments in histogram form in Fig. 29. The population from the NS give values of $Fr_0 \sim 0.49 \pm 0.09$, which is similar to the value of 0.56 calculated from potential flow for a square periodic lattice of bubbles. However, this agreement may be fortuitous because Fr_0 does not use the actual diluted bubble density due to entrainment and diffusion. When the actual bubble densities are used, the NS give $Fr \sim 0.94 \pm 0.06$ which agrees with the previous experiments: Lewis⁷ reported $Fr \sim 1.1$, Glimm and Li⁴⁶ found $Fr \sim 1.1$ for the RR,²⁴ and the LEM experiments³⁰ obtain $Fr \sim 0.89 \pm 0.08$, all assuming no entrainment. Scorer⁸ found a significant amount of entrainment in rising plumes and deduced $Fr \sim 1.2$.

To summarize, the NS clearly show that the bubbles have entrained heavy fluid and these exhibit a $Fr \sim 0.94$ in agreement with experiments. Such a value disagrees with the $\sim 1/2$ obtained from a potential flow model for a bubble in a tight tube¹⁰ or a square periodic lattice.¹² This may be due to

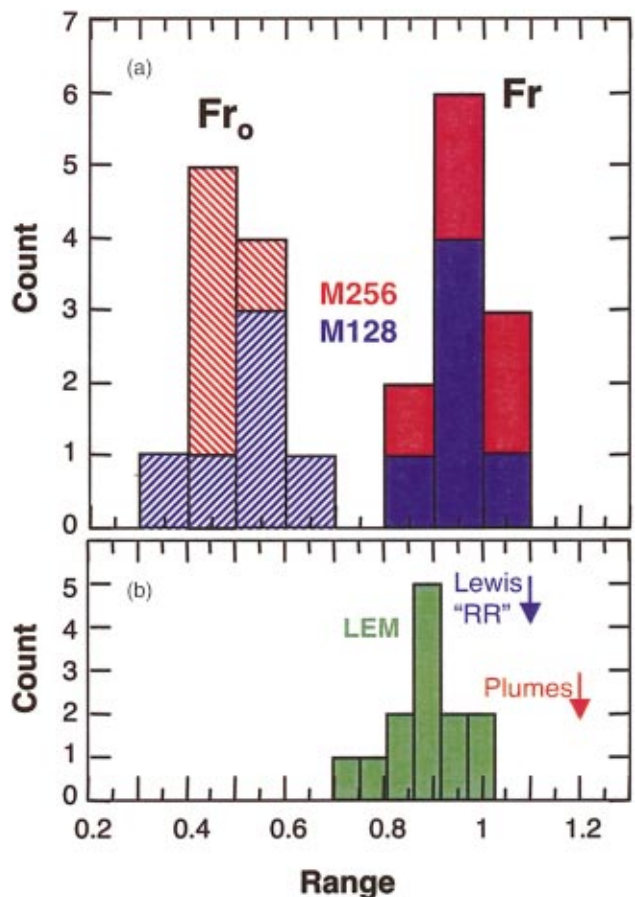


FIG. 29. (Color) Asymptotic Froude-type number of dominant bubbles from (a) NS and (b) experiments.

an envelope instability^{32,46} or to the fact that RT bubbles resemble isolated bubbles in an open bath rather than in a tight tube or array. Remember, Davies and Taylor⁶ found that Fr increased from $1/2$ to $2/3$ for lenticular bubbles when the container was enlarged. The physical basis for this behavior is that the spike counterflow velocity is significantly larger when the boundaries are nearby and this increases the drag on the bubbles.⁹ For RT bubbles, Fr may exceed $2/3$ because they are more cylindrical (ellipsoidal) rather than lenticular and such bodies have yet smaller drag coefficients.⁵⁸

VI. ENERGY BUDGET

A complementary method for estimating α_b involves global energy balance since the overturning of density due to RT mixing in the gravitational field releases potential energy depending only on the horizontally averaged vertical density profile $\langle \rho \rangle$. For $A \sim 0$, $\langle \rho \rangle$ is nearly symmetric in Z with $h_b \sim h_s = h$ and $\langle \rho \rangle$ varies almost linearly between ρ_h and ρ_l . This is a reasonable approximation as seen in Fig. 7. Then, the decrease in potential energy becomes

$$\delta P = \int_{-h}^0 (\rho_l - \langle \rho \rangle) g z dz + \int_0^h (\langle \rho \rangle - \rho_h) g z dz \sim \frac{(\rho_h - \rho_l) g h^2}{6}. \quad (25)$$

The directed kinetic energy is more difficult to evaluate because the density and velocity fluctuations are correlated. However, for $\rho_h \sim \rho_l$ the densities can be replaced by their average with only a minor error and the average velocity can be estimated by $V_z \sim h$. This gives a vertical kinetic energy of

$$K_z = \frac{1}{2L^2} \int_{-h}^h \rho V_z^2 dx dy dz = \frac{\rho_l + \rho_h}{2} h^2 h \quad (26)$$

and a ratio

$$\frac{K_z}{\delta P} = \frac{3h^2}{Ag h} = 12\alpha_b. \quad (27)$$

This implies an upper bound of $\alpha_b \sim 0.08$ if there are no other energy sinks, i.e., if $K_z \sim \delta P$.

However, the dissipated energy E_d and the kinetic energy in the horizontal directions K_x and K_y must also be considered because they affect the global energy balance by

$$\delta P = K_z + K_x + K_y + E_d \equiv K + E_d. \quad (28)$$

The ratio of total kinetic and potential energies in the NS is represented by the dark histogram in Fig. 30. The NS obtain $K/\delta P \sim 0.46 \pm 0.04$ which means that more than 50% of the liberated energy is dissipated. The ratio of $K_x + K_y$ to K_z is also represented in Fig. 30 by the light histogram and has a sample average of 0.58 ± 0.04 . Combining energy balance with Eq. (27) yields

$$\alpha_b \sim \frac{K/\delta P}{12[1 + (K_x + K_y)/K_z]}. \quad (29)$$

With no energy dissipation $K/\delta P \sim 1$, Eq. (28) yields $\alpha_b \sim 0.053$ for $(K_x + K_y)/K_z \sim 0.58$ in agreement with experimental measurements. With the observed $K/\delta P \sim 0.46$ in these NS, Eq. (29) yields $\alpha_b \sim 0.024$ which is consistent with our simulation results. A code by code comparison is shown in Fig. 31 by plotting the observed α_b with that calculated from Eq. (29). Again, there is reasonable agreement on the sample average of α_b , but there is a single point outside the error bars at $\alpha_b = (0.02, 0.03)$ from ALEGRA with IR. The calculated value from Eq. (29) is low $\alpha_b = 0.02$ because the kinetic energy is low $K/\delta P \sim 0.38$. This is currently not understood except to say that the ALEGRA calculation with IR is the shortest in terms of $Ag t^2 / \lambda_p$ and may have not yet reached an asymptotic state.

Within this picture, energy dissipation is identified for the reduced α_b obtained in the NS. This may be reconciled with the observed buoyancy reduction described in Sec. V if species diffusion can be related to energy dissipation.

VII. FLUCTUATION SPECTRA

The fluctuations are analyzed by Fourier transforming the volume fraction in the horizontal plane at the original interface. Late time images of f_l at $Z=0$ are shown in Fig. 32 for the specified NS. The NS in the top row are for M256 and exhibit much more fine scale features than those in the bottom row for M128. The NS without IR have significant molecular mixing (gray) and this is manifested with a

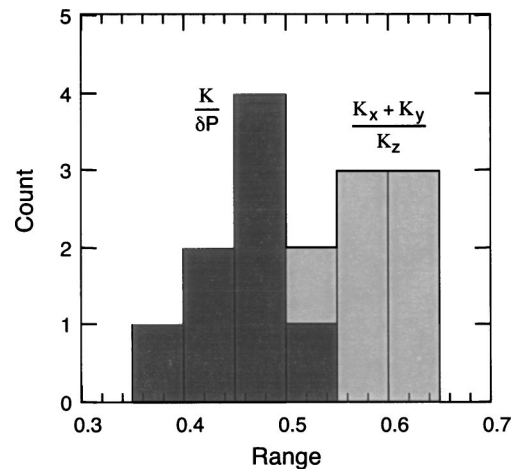


FIG. 30. Histogram of energy ratios: kinetic/potential= $K/\delta P$ and horizontal/vertical= $(K_x + K_y)/K_z$.

smaller variance $\langle f_l^2 \rangle - \langle f_l \rangle^2 \sim 0.05$ than 0.18 with IR. But, even though IR keeps the fluids segregated, the correlation of velocity and density indicates that there is co-moving light and heavy (entrained) fluid and this is manifested with $\rho_b \sim 2 \text{ g/cm}^{-3}$. In addition, IR does seem to enhance small scale features.

The scale distribution is characterized here by the “power spectrum”

$$\Phi(N) \equiv 2\pi N \langle f_l(N)^2 \rangle_\theta, \quad (30)$$

where $\langle f_l(N)^2 \rangle_\theta$ is the azimuthal average (in k -space) of the square of the Fourier transform $f_l(N)$ and N is the mode number $kL/2\pi$. With this normalization, the sum of $\Phi(N)$ from $N=1$ to the Nyquist limit ($Ny=256/2$ or $128/2$) equals the variance of f_l , namely,

$$\langle f_l^2 \rangle - \langle f_l \rangle^2 = \sum_{N=1}^{Ny} \Phi(N). \quad (31)$$

Figure 33 compares $\Phi(N)$ from the various NS with the standard color coding at (a) early and (b) late times. The spectral peaks decrease from $N \sim 4-10$ in (a) to 2-3 in (b)

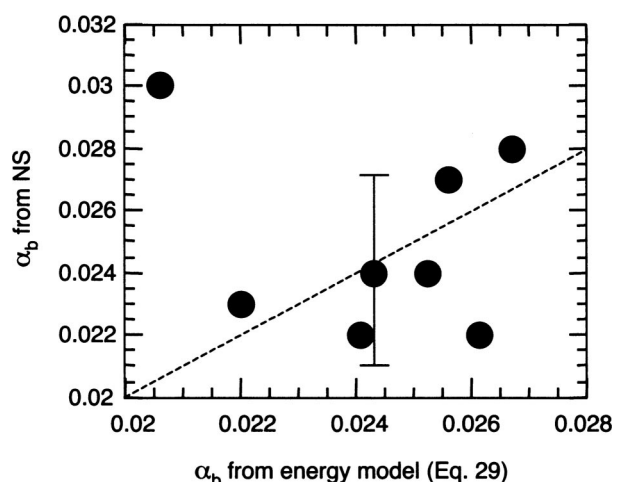
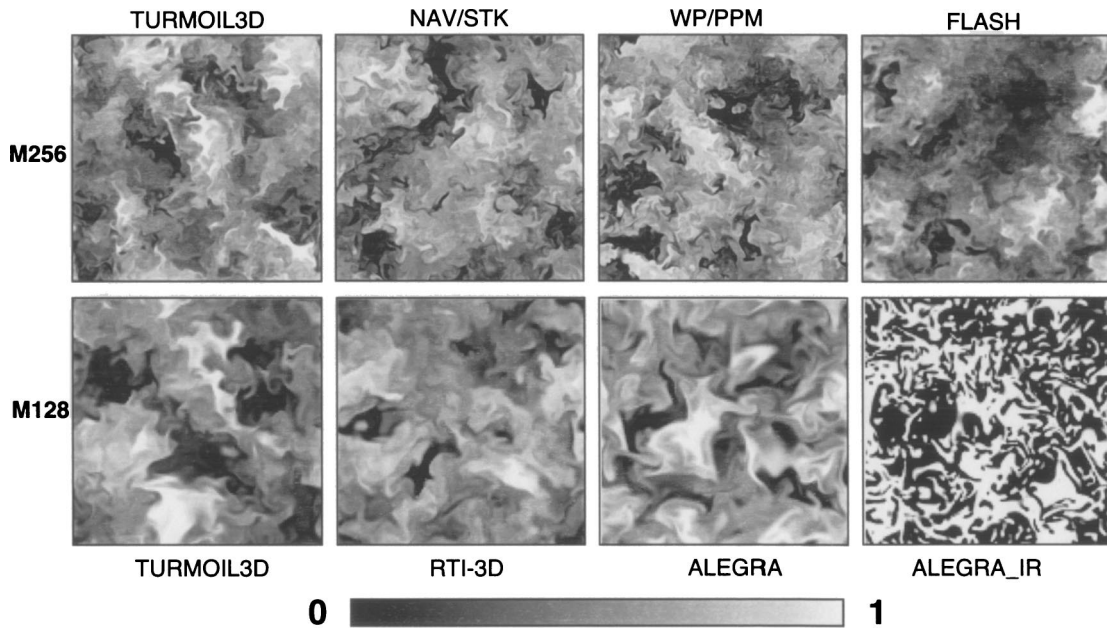


FIG. 31. Comparison of α_b from NS and energy model Eq. (29).

FIG. 32. Volume fraction of “light” fluid at $Z=0$ for late time.

consistent with the self-similar evolution of λ_b observed earlier. Then the spectra exhibit a region of Kolmogorov type behavior as $N^{-5/3}$ (gray line). In the later stages when the separation between the inertial $\sim \lambda_b$ and dissipation scales is large, the spectral index is found to be -1.4 to -1.8 . Above some critical mode number N_{crt} , the spectra decrease precipitously with indices in the range -3 to -5 except for -10 for FLASH. N_{crt} is defined by the intersection point of the $N^{-5/3}$ region and a power law fit (line on log–log plot) to the dissipative part of the spectrum.

N_{crt} compares favorably to the Kolmogorov mode number $N_{\text{Kol}} = L/\lambda_{\text{Kol}}$, where

$$\lambda_{\text{Kol}} = (v^3/\epsilon)^{1/4}. \quad (32)$$

The specific dissipation rate/volume is taken to be

$$\epsilon \sim \frac{1}{\rho_l + \rho_h} \frac{d}{dt} \left(\frac{E_d}{2h} \right) \sim \left(1 - \frac{K}{\delta P} \right) \frac{Ag}{12} \frac{dh}{dt}. \quad (33)$$

Then, with the amplitude given by Eq. (1), the kinetic and potential energies described in the previous section, and the numerical viscosity given by Eq. (8), we obtain

$$\lambda_{\text{Kol}} \sim \left(\frac{6\varpi^3}{(1-K/\delta P)\alpha_b} \right)^{1/4} \left(\frac{\Delta}{Agt^2} \right)^{1/8} 2\pi\Delta. \quad (34)$$

λ_{Kol} depends mainly on the viscosity through ϖ and Δ , and is typically 3–5 zones wide. As shown in Fig. 34, $N_{\text{Kol}} = L/\lambda_{\text{Kol}}$ is found to increase linearly with N_{crt} with a correlation coefficient ~ 0.9 . This implies that the numerical viscosities obtained from the single mode study accurately govern energy dissipation since the slopes $N_{\text{crt}}/N_{\text{Kol}}$ are near unity (1.02 early and 1.05 late).

It is interesting to note that the most unstable mode λ_p with viscosity is almost identical to λ_{Kol} . This can be seen by comparing Eqs. (15) and (34), namely,

$$\frac{\lambda_p}{\lambda_{\text{Kol}}} \sim \left(\frac{(1-K/\delta P)\alpha_b}{6} \right)^{1/4} \left(\frac{Agt^2}{\Delta} \right)^{1/8} \frac{2}{\varpi^{1/12}} \sim 1. \quad (35)$$

This is physically reasonable and supports the use of the well known single mode evolution to quantitatively evaluate the numerical viscosity.

It is also interesting to note that if the well resolved (low N) portion of the spectrum is an accurate representation of what should be a Kolmogorov spectrum, it is possible to estimate how well the NS perform as the zoning is varied. This is done by comparing the actual variance of f_l given by Eq. (31) to the ideal variance in the limit of zero viscosity, namely,

$$(\langle f_l^2 \rangle - \langle f_l \rangle^2)_{\text{Ideal}} = \sum_{N=1}^{N_{\text{crt}}} \Phi(N) + \sum_{N_{\text{crt}}+1}^{\infty} c N^{-5/3}, \quad (36)$$

where the constant c is obtained by fitting $N^{-5/3}$ to the computed spectrum for $N < N_{\text{crt}}$. Then, the fraction of the variance of f_l described by the NS can be estimated as

$$\frac{\langle f_l^2 \rangle - \langle f_l \rangle^2}{(\langle f_l^2 \rangle - \langle f_l \rangle^2)_{\text{Ideal}}} = \frac{\sum_{N=1}^{N_{\text{crt}}} \Phi(N)}{\sum_{N=1}^{N_{\text{crt}}} \Phi(N) + \sum_{N_{\text{crt}}+1}^{\infty} c N^{-5/3}}. \quad (37)$$

Remember, the variance in the NS is represented by the numerator and an ideal Kolmogorov variance with no dissipation is represented by the denominator. This “explained fraction” is shown in Fig. 35(a) and Table V to increase with $N_{\text{crt}} \propto N_{\text{Kol}} \propto L/\Delta$. The late points (solid) have an average $\sim 91\%$ compared to $\sim 78\%$ earlier in time (open) because the spectra have broadened due to the self-similar growth of the inertial range. Please note the 50% offset in the ordinate since this analysis is not meaningful for narrow spectra $N_{\text{crt}} \ll 10$.

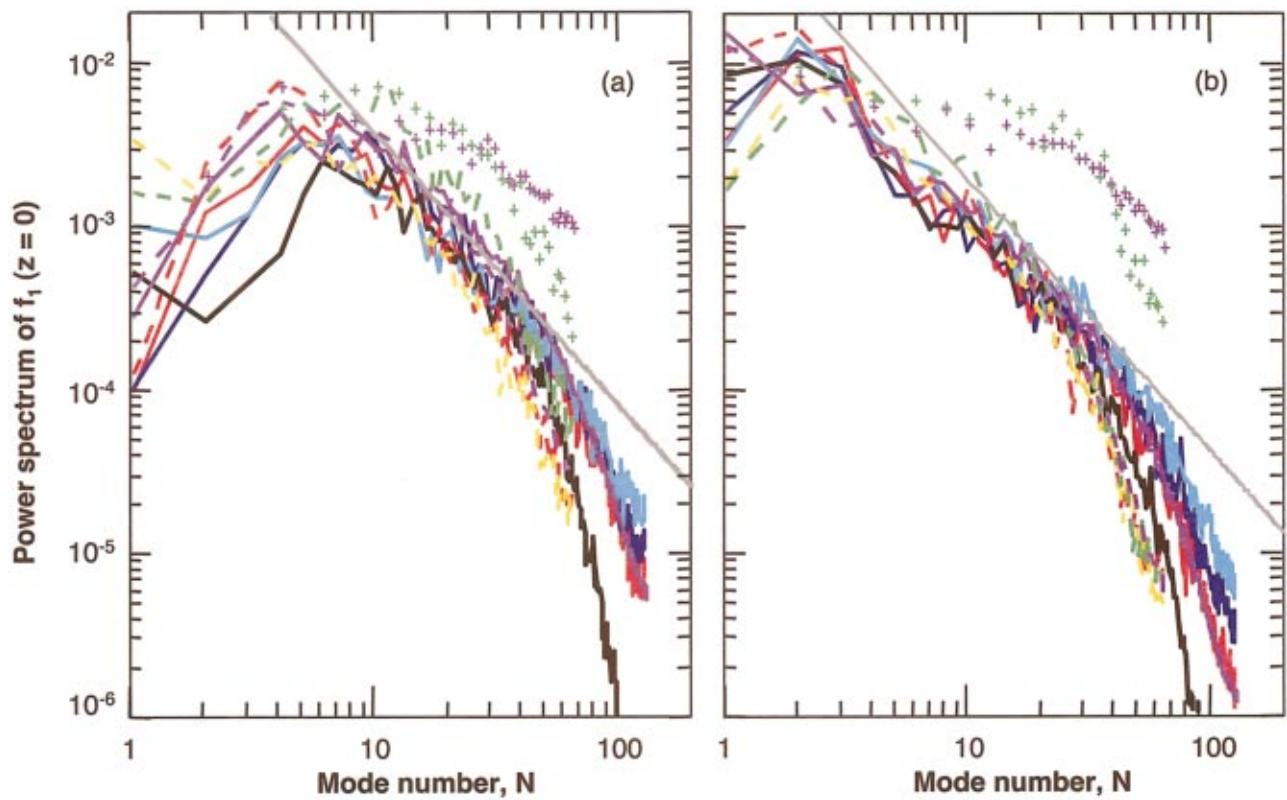


FIG. 33. (Color) Power spectrum of volume fraction at original interface $Z=0$ for (a) early and (b) late times using standard color coding. Gray line represents Kolmogorov-type spectrum $\propto N^{-5/3}$.

The lines are calculated for an ideal Kolmogorov spectrum as

$$\frac{\langle f_l^2 \rangle - \langle f_l \rangle^2}{(\langle f_l^2 \rangle - \langle f_l \rangle^2)_{\text{ideal}}} = \frac{\sum_{N_{\min}}^{N_{\text{crit}}} N^{-5/3}}{\sum_{N_{\min}}^{\infty} N^{-5/3}} \quad (38)$$

by assuming that there is zero contribution below the inertial range $N < N_{\min} \sim L/\lambda_b - 1$ and from the dissipative part of the spectrum $N > N_{\text{Kol}}$. The late (solid) points lie between the

$N_{\min} \sim 1-2$ lines and the early (open) points agree with $N_{\min} \sim 5$ consistent with the spectra in Fig. 33. The points and lines in Fig. 35(a) can be consolidated by plotting the “explained fraction” vs N_{crit}/N_{\min} because it represents the important dynamic range between the inertial and dissipation scales. From Fig. 33, N_{\min} for the NS is taken as 4 and 1 for the early and late data, respectively. The agreement is surprising given the simplifying assumptions and the variation suggests two important points. First, the strong initial increase suggests that the spectral width must exceed $N_{\text{crit}}/N_{\min} \sim \lambda_b/\lambda_{\text{Kol}} \sim 5-10$ to obtain an accurate ($>50\%$) representation of RT turbulence. Second, it is numerically costly to obtain $>95\%$ accuracy since the improvement in performance with $N_{\text{crit}} \sim N_{\text{Kol}} \propto \Delta^{-9/8}$ is weak. For example, the zoning would have to be increased almost tenfold to recover the 5% not described by these $256 \times 256 \times 512$ simulations.

VIII. SUMMARY AND DISCUSSION

This paper describes a comparative study of the multi-mode RT instability in the limit of strong mode coupling. This is done by imposing only short wavelength perturbations so that the asymptotic self-similar evolution to longer wavelengths progresses solely by the nonlinear coupling of saturated modes. This study is performed with a variety of MILES described in Sec. II from different institutions by quantitatively comparing the results with theory and experiments from the viewpoint of single mode growth, self-similar bubble dynamics, energy balance and spectral analy-

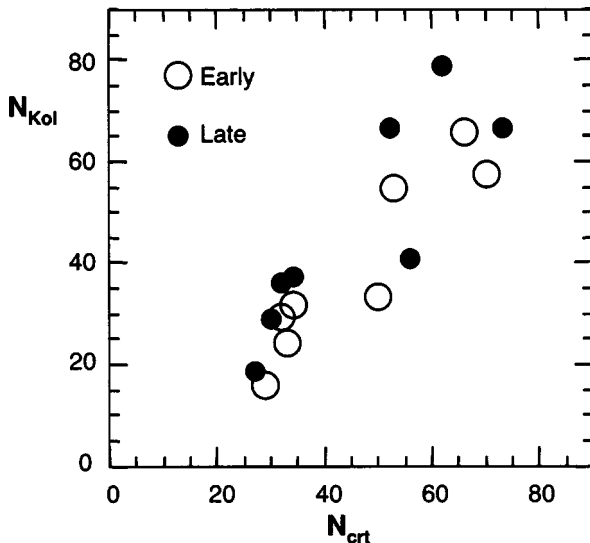


FIG. 34. Critical mode number N_{crit} vs Kolmogorov mode number N_{Kol} .

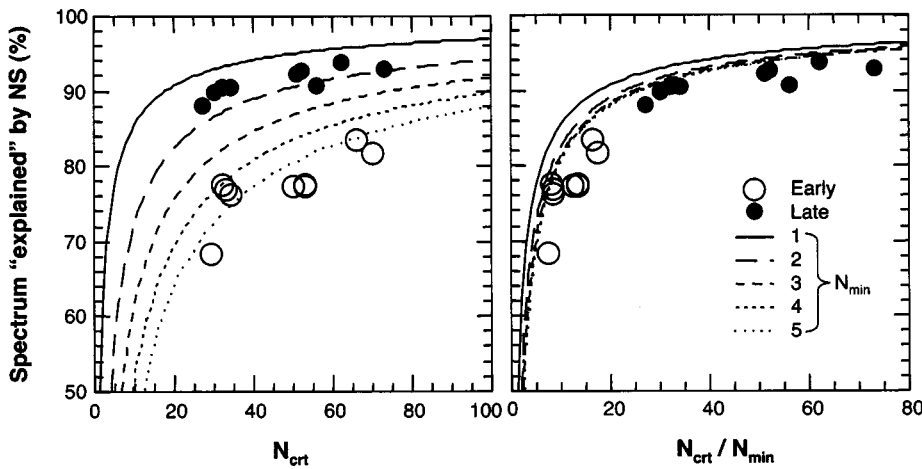


FIG. 35. Fraction of ideal Kolmogorov spectrum described by NS. Lines given by Eq. (38).

sis. The numerical results are found to be converged by zoning, physically self-consistent and in reasonable agreement with previous direct NS (DNS), experiments and theory. The main difference is that the bubble acceleration parameter is found to be $\alpha_b \sim 0.025 \pm 0.003$ [when the original A is used in Eq. (1)] compared to $\alpha_b \sim 0.057 \pm 0.008$ in the experiments. It is possible that this difference is due to numerical artifacts, but we believe that α_b from these NS is only the contribution from mode coupling and represents a lower bound. We study this limit first because the associated α_b should be insensitive to the initial conditions since it is dominated by the non-linear interaction of short wavelength modes of “intrinsic” scales ($h_k \sim \lambda$) near saturation. We consider it to be fundamentally important to know if this growth coupling limit represents the typical experimental conditions because it would affect mix models. However, this limit is stressful computationally because the parent modes couple nonlinearly to both shorter and longer wavelength modes and the former produce significant fine-scale entrainment or diffusion. When the fine-scale dilution of the bubbles is accounted for as described in Sec. V and discussed below, the NS and experiments are in better agreement. In the experiments, the larger α_b could be due to a smaller amount of

fine-scale dilution and/or the presence of long wavelengths perturbations with amplitude $> 10^{-4}/k$,^{20,21,31,34,40,49} and these may be related. Clearly, more simulations⁷⁹ and measurements are ultimately required to clarify these issues. Our results are summarized as follows.

The NS are first compared with theory by conducting 3D single mode zoning studies as described in Sec. III. At small amplitude, the observed exponential growth rate Γ is typically better than 80% of classical when there are more than 8 zones/ λ . For fewer zones, a numerical viscosity $v \propto \sqrt{g\Delta^3}$ is inferred by fitting the analytical Γ with that observed. At large amplitude, the bubble terminal velocity is found to be within 90% of that predicted by potential flow when there are more than 8 zones/ λ .

The multimode study was designed to investigate the mode-coupling limit by imposing only short wavelength perturbations: modes 32–64 for $256 \times 256 \times 512$ zones and 16–32 for $128 \times 128 \times 256$ zones. In the initial phase $Agt^2 < 100\lambda_p$, the growth is rapid due to the amplification of the imposed modes and consistent with the marginally resolved single mode growth rate at ~ 8 zones/ λ . Subsequently, the flow is dominated by longer wavelength modes that have grown self-similarly via mode coupling. Since these modes are better resolved, the NS are expected to be even more accurate in this phase. As a result, the two zone resolutions give the same asymptotic values of α_b .

The fidelity of the multimode NS is evaluated by conducting a spectral analysis of the volume fraction fluctuations at the midplane as described in Sec. VII. The NS without IR exhibit Kolmogorov power spectra (index $\sim -5/3$) between the inertial range λ_b and the dissipation scale. The latter agrees with the Kolmogorov scale $\lambda_{Kol} \sim 3\Delta$ calculated with our numerical viscosity inferred from linear theory. Since λ_b grows with h_b , the spectral dynamic range increases to $\lambda_b/\lambda_{Kol} \sim 60$ near the end of the NS and this implies that our NS resolve over 90% of the fluctuations compared to an idealized ($v=0$) Kolmogorov spectrum.

It is found that the scale at which energy is dissipated is proportional to the zone size but the amount of dissipation remains constant at $\sim 50\%$ of the converted potential energy in agreement with true DNS.⁷⁸ This is important since it is

TABLE V. Energy budget and spectral characteristics.

Simulation	Kinetic/potential energies (%)		Actual/ideal f_1 variance (%)		
	Early	Late	N_{crt}	N_{Kol}	Ratio
$256 \times 256 \times 512$					
TURMOIL3D	50	52	62	79	94
FLASH	33	47	51		92
NAV/STK	47	45	56	41	91
WP/PPM	39	48	73	67	93
HYDRA	43	41	52	67	93
$128 \times 128 \times 256$					
TURMOIL3D	54	49	32	36	90
RTI-3D	39	43	34	38	91
ALEGRA	41	46	27	19	88
ALEGRA_IR	40	38			
HYDRA	38	41	30	29	90
HYDRA_IR	36	37			

possible at small A to link α_b to the directed kinetic/potential energy as described in Sec. VI.

The multimode NS are also compared to models of self-similar bubble dynamics (Secs. I and V) because the models have been important in understanding the RT instability. The cornerstone of these models is the well known (and accepted) terminal bubble velocity Eq. (2) which depends on the bubble size D_b or λ_b , the effective density contrast $\delta\rho$ and the proportionality constant Fr. If $D_b \propto h_b$, then Eq. (1) solves Eq. (2) with $\alpha_b \propto \text{Fr}^2 \delta\rho D_b/h_b$ [e.g., Eq. (3)]. Such self-similar growth can occur by (1) coupling of smaller saturated bubbles or (2) amplification of ambient modes of successively longer λ . The first is a merger process that is insensitive to the initial conditions because it involves the nonlinear coupling of modes with “intrinsic” scales $h_k \sim \lambda$ near saturation. The second is a competition process that depends weakly on the initial perturbations because the small amplitude growth is exponential. In these simulations, the diameter of the dominant bubbles is obtained by autocorrelation analysis (Sec. V) and it is found to increase self-similarly $D_b/h_b \sim 0.38 \pm 25\%$ in agreement with LEM measurements³⁰ $D_b/h_b \sim 0.41 \pm 15\%$ near $A \sim 0.5$.

However, in order to describe the velocity of the dominant bubbles and thus α_b , it is necessary to account for the density dilution due to small-scale mixing or entrainment. This is quantified in Fig. 29 in terms of the proportionality constant Fr in Eqs. (2), (23), and (24). In these NS, we obtain $\text{Fr} \sim 0.49$ by assuming bubbles with the original density $\rho_b = \rho_l$ and $\text{Fr} \sim 0.94$ by using the actual diluted bubble density $\rho_b \sim 2-2.5 \rho_l$. In RT experiments, it was found that $\text{Fr} \sim 0.9-1.1$ (Refs. 7, 30, 46) assuming no fine-scale mixing or entrainment because of the significant surface tension. For highly miscible plumes,⁸ a value of $\text{Fr} \sim 1.2$ was obtained when normalized for the observed density dilution. These results indicate that the our NS without IR exhibit significant fine-scale mixing similar to true DNS,⁷⁸ miscible plumes,⁸ and miscible RT experiments.^{77,80} In our NS with IR, fine-scale mixing is replaced by an equivalent entrainment and this leads to similar values of ρ_b and thus α_b . The dilution may have been small in most of the RT experiments²⁴⁻³⁰ reporting an α_b because of the high Schmidt number or surface tension. For example, in the LEM experiments,³⁰ α_b increased by only 20% when the surface tension was increased 50-fold.

These issues are not yet resolved and should be investigated both numerically and experimentally. For example, simulations with various front-tracking methods would be very useful in investigating the effect of fine-scale mixing and entrainment. However, these effects may depend on the initial conditions.^{21,40} Inogamov²¹ suggests that true self-similar behavior (α_b independent of time) occurs only for an initial k^{-2} spectrum and that α_b increases logarithmically with the initial amplitude. Simulations by Linden *et al.*⁴⁰ suggest that α_b can be increased from $\alpha_b \sim 0.035$ by adding long wavelength modes with amplitude $\geq 0.001\lambda$. Modes with amplitude $\geq 0.01\lambda$ must be added when $\alpha_b \sim 0.06$. Dimonte⁴⁹ attempts to quantify the dependence of α_b and λ_b/h_b on initial conditions by applying Haan’s saturation model^{50,51} to bubble dynamics. With large long wavelength

perturbations, the fine-scale dilution that characterizes the mode-coupling limit may be reduced since the nonlinear coupling to short wavelength modes is smaller. In experiments, it is important to measure the initial conditions, but this may be difficult because they are small and may be augmented in transit by vibrations.⁴⁹ In addition, fine-scale mixing would best be measured directly with reactive fluids because methods employing laser sheets are prone to error when the laser intensity is not uniform in both directions.

Finally, if anyone is interested in repeating these calculations with their own numerical methods, please contact dimonte@lanl.gov or any of the other authors for an electronic form of the initial conditions.

ACKNOWLEDGMENTS

This work was performed under the auspices of the U.S. Department of Energy (DOE) by Los Alamos National Laboratory under Contract No. W-7405-ENG-36, by Lawrence Livermore National Laboratory under Contract No. W-7405-ENG-48, and by Sandia National Laboratory under Contract No. DE-AC04-94AL85000. The work at Texas A&M University was supported by the U.S. DOE under Awards Nos. DE-FG03-099DP-00277 and DE-FG03-02NA00060.

- ¹Lord Rayleigh, *Scientific Papers II* (Cambridge University Press, Cambridge, 1900), p. 200.
- ²G. I. Taylor, “The instability of liquid surfaces when accelerated in a direction perpendicular to their plane,” Proc. R. Soc. London, Ser. A **201**, 192 (1950).
- ³S. Chandrasekhar, *Hydrodynamic and Hydromagnetic Stability* (Oxford University Press, Oxford, 1961).
- ⁴H. W. Emmons, C. T. Chang, and B. C. Watson, “Taylor instability of finite surface waves,” J. Fluid Mech. **7**, 177 (1960).
- ⁵D. T. Dumitrescu, “Stromung einer Luftblase im senkrecht Rohr,” Z. Angew. Math. Mech. **23**, 139 (1943).
- ⁶R. M. Davies and G. I. Taylor, “The mechanics of large bubbles rising through extended liquids and through liquids in tubes,” Proc. R. Soc. London, Ser. A **200**, 375 (1950).
- ⁷D. J. Lewis, “The instability of liquid surfaces when accelerated in direction perpendicular to their planes,” Proc. R. Soc. London, Ser. A **202**, 81 (1950).
- ⁸R. S. Scorer, “Experiments on convection of isolated masses of buoyant fluid,” J. Fluid Mech. **2**, 583 (1957).
- ⁹R. Collins, “The effect of a containing cylindrical boundary on the velocity of a large gas bubble in a liquid,” J. Fluid Mech. **28**, 97 (1967).
- ¹⁰D. Layzer, “On the instability of superposed fluids in a gravitational field,” Astrophys. J. **122**, 1 (1955).
- ¹¹H. J. Kull, “Theory of the Rayleigh–Taylor instability,” Phys. Rep. **206**, 197 (1991).
- ¹²J. Hecht, U. Alon, and D. Shvarts, “Potential flow models of Rayleigh–Taylor and Richtmyer–Meshkov bubble fronts,” Phys. Fluids **6**, 4019 (1994).
- ¹³G. Tryggvason and S. O. Unverdi, “Computations of three-dimensional Rayleigh–Taylor instability,” Phys. Fluids A **2**, 656 (1990).
- ¹⁴X. L. Li, “Study of three-dimensional Rayleigh–Taylor instability in compressible fluids through level set method and parallel computation,” Phys. Fluids A **5**, 1904 (1993).
- ¹⁵X. L. Li, “A numerical study of three-dimensional bubble merger in the Rayleigh–Taylor instability,” Phys. Fluids **8**, 336 (1996).
- ¹⁶X. L. Li, B. X. Jin, and J. Glimm, “Numerical study of 3D Rayleigh–Taylor instability through the TVD/AC scheme and parallel computation,” J. Comput. Phys. **126**, 343 (1996).
- ¹⁷J. Hecht, D. Offer, U. Alon, D. Shvarts, S. A. Orszag, and R. L. McCrory, “Three-dimensional simulations and analysis of the nonlinear stage of the Rayleigh–Taylor instability,” Laser Part. Beams **13**, 423 (1995).
- ¹⁸X. He, R. Zhang, S. Chen, and G. Doolen, “On the three-dimensional Rayleigh–Taylor instability,” Phys. Fluids **11**, 1143 (1999).

- ¹⁹K. Kadau, T. Germann, N. Hadjiconstantinou, P. Lambdahl, G. Dimonte, B. L. Holian, and B. Alder, "Nanohydrodynamics simulations: An atomistic view of the Rayleigh–Taylor instability," *Proc. Natl. Acad. Sci. U.S.A.* (to be published).
- ²⁰G. Birkhoff, "Taylor instability and laminar mixing," University of California Report No. LA-1862, 1955.
- ²¹N. A. Inogamov, "Turbulent stage of the Rayleigh–Taylor instability," *Sov. Tech. Phys. Lett.* **4**, 299 (1978).
- ²²N. A. Inogamov, A. V. Chekhlov, Al. Yu. Dem'yanov, S. I. Anisimov, and O. M. Belotserkovskii, in *Proceedings of the Third International Workshop on Physics Compressible Turbulent Mixing*, edited by R. Dautray (Commissariat Energie Atomique, Cesta, France, 1991), p. 409.
- ²³N. N. Anuchina, Yu. A. Kucherenko, V. E. Neuvazhaev, V. N. Ogibina, L. I. Shibareshov, and V. G. Yakovlev, "Turbulent mixing at an accelerating interface between liquids of different densities," *Izv. Akad. Nauk SSSR, Mekh. Zhidk. Gaza* **6**, 157 (1978).
- ²⁴K. I. Read, "Experimental investigation of turbulent mixing by Rayleigh–Taylor instability," *Physica D* **12**, 45 (1984).
- ²⁵D. L. Youngs, "Modeling turbulent mixing by Rayleigh–Taylor instability," *Physica D* **37**, 270 (1989).
- ²⁶M. J. Andrews and D. B. Spalding, "A simple experiment to investigate two-dimensional mixing by Rayleigh–Taylor instability," *Phys. Fluids A* **2**, 922 (1990).
- ²⁷Yu. A. Kucherenko, L. I. Shibareshov, V. I. Chitaikin, S. I. Balabin, and A. P. Pylaev, "Experimental study of the gravitational turbulent mixing self-similar mode," in *Proceedings of the Third International Workshop on Physics Compressible Turbulent Mixing*, edited by R. Dautray (Commissariat Energie Atomique, Cesta, France, 1991), p. 427.
- ²⁸G. Dimonte and M. Schneider, "Turbulent Rayleigh–Taylor instability experiments with variable acceleration," *Phys. Rev. E* **54**, 3740 (1996).
- ²⁹M. Schneider, G. Dimonte, and B. Remington, "Large and small scale structure in Rayleigh–Taylor mixing," *Phys. Rev. Lett.* **80**, 3507 (1998).
- ³⁰G. Dimonte and M. Schneider, "Density ratio dependence of Rayleigh–Taylor mixing for sustained and impulsive acceleration histories," *Phys. Fluids* **12**, 304 (2000).
- ³¹D. L. Youngs, "Numerical simulation of turbulent mixing by Rayleigh–Taylor instability," *Physica D* **12**, 32 (1984).
- ³²J. Glimm, X. L. Li, R. Menikoff, D. H. Sharp, and Q. Zhang, "A numerical study of bubble interactions in Rayleigh–Taylor instability for compressible fluids," *Phys. Fluids A* **2**, 2046 (1990).
- ³³N. Freed, D. Ofer, D. Shvarts, and S. O. Orszag, "Two-phase flow analysis of self-similar turbulent mixing by Rayleigh–Taylor instability," *Phys. Fluids A* **3**, 912 (1991).
- ³⁴C. Cherfils and K. O. Mikaelian, "Simple model for the turbulent mixing width at an ablating surface," *Phys. Fluids* **8**, 522 (1996).
- ³⁵N. N. Anuchina, V. A. Gordeichuk, N. S. Eskov, O. S. Ilyutina, O. M. Kozyrev, and V. I. Volkov, in *Proceedings of the 6th International on Workshop Physics Compressible Turbulent Mixing*, edited by G. Jourdan and L. Houas (Imprimerie Caractere, Marseille, France, 1997), p. 24.
- ³⁶X. He, S. Chen, and R. Zhang, "A lattice Boltzmann scheme for incompressible multiphase flow and its application in simulation of Rayleigh–Taylor instability," *J. Comput. Phys.* **152**, 642 (1999).
- ³⁷T. Clark, "A numerical study of the statistics of a 2D Rayleigh–Taylor mixing layer," *Phys. Fluids* **15**, 2413 (2003).
- ³⁸D. L. Youngs, "Three-dimensional numerical simulation of turbulent mixing by Rayleigh–Taylor instability," *Phys. Fluids A* **3**, 1312 (1991).
- ³⁹D. L. Youngs, "Numerical simulation of mixing by Rayleigh–Taylor and Richtmyer–Meshkov instabilities," *Laser Part. Beams* **12**, 725 (1994).
- ⁴⁰P. F. Linden, J. M. Redondo, and D. L. Youngs, "Molecular mixing in Rayleigh–Taylor instability," *J. Fluid Mech.* **265**, 97 (1994).
- ⁴¹A. W. Cook and P. E. Dimotakis, "Transition stages of Rayleigh–Taylor instability between miscible fluids," *J. Fluid Mech.* **443**, 69 (2001).
- ⁴²Y.-N. Young, H. Tufo, A. Dubey, and R. Rosner, "On the miscible Rayleigh–Taylor instability: Two and three dimensions," *J. Fluid Mech.* **447**, 377 (2001).
- ⁴³J. Glimm, J. W. Grove, X. L. Li, W. Oh, and D. H. Sharp, "A critical analysis of Rayleigh–Taylor growth rates," *J. Comput. Phys.* **169**, 652 (2001); E. George, J. Glimm, X.-L. Li, A. Marchese, and Z.-L. Xu, "A comparison of experimental theoretical, and numerical simulation Rayleigh–Taylor mixing rates," *Proc. Nat. Acad. Sci., U.S.A.* **99**, 2587 (2002).
- ⁴⁴D. Oron, L. Arazi, D. Kartoon, A. Rikanati, U. Alon, and D. Shvarts, "Dimensionality dependence of Rayleigh–Taylor and Richtmyer–Meshkov instability late-time scaling laws," *Phys. Plasmas* **8**, 2883 (2001).
- ⁴⁵J. A. Zufiria, "Bubble competition in Rayleigh–Taylor instability," *Phys. Fluids* **31**, 440 (1988).
- ⁴⁶J. Glimm and X. L. Li, "Validation of Sharp–Wheeler merger model from experimental and computational data," *Phys. Fluids* **31**, 2077 (1988).
- ⁴⁷D. Shvarts, U. Alon, D. Ofer, R. L. McCrory, and C. P. Verdon, "Nonlinear evolution of multimode Rayleigh–Taylor instability in two and three dimensions," *Phys. Plasmas* **2**, 2465 (1995).
- ⁴⁸U. Alon, J. Hecht, D. Ofer, and D. Shvarts, "Power laws and similarity of Rayleigh–Taylor and Richtmyer–Meshkov mixing fronts at all density ratios," *Phys. Rev. Lett.* **74**, 534 (1995).
- ⁴⁹G. Dimonte, "Dependence of turbulent Rayleigh–Taylor (RT) instability on initial conditions," *Phys. Rev. E* (to be published).
- ⁵⁰S. W. Haan, "Onset of nonlinear saturation for Rayleigh–Taylor growth in the presence of a full spectrum of modes," *Phys. Rev. A* **39**, 5812 (1989).
- ⁵¹S. W. Haan, "Weakly nonlinear hydrodynamic instabilities in inertial fusion," *Phys. Fluids B* **3**, 2349 (1991).
- ⁵²J. C. Hanson, P. A. Rosen, T. J. Goldsack, K. Oades, P. Fieldhouse, N. Cowperthwaite, D. L. Youngs, N. Mawhinney, and A. J. Baxter, "Radiation driven planar foil instability and mix experiments at the AWE HELEN laser," *Laser Part. Beams* **8**, 51 (1990).
- ⁵³J. Glimm, D. Saltz, and D. H. Sharp, "Statistical evolution of chaotic fluid mixing," *Phys. Rev. Lett.* **80**, 712 (1998).
- ⁵⁴J. D. Ramshaw, "Simple model for linear and nonlinear mixing at unstable fluid interfaces with variable acceleration," *Phys. Rev. E* **58**, 5834 (1998).
- ⁵⁵G. Dimonte, "Spanwise homogeneous buoyancy-drag model for Rayleigh–Taylor mixing and experimental verification," *Phys. Plasmas* **7**, 2255 (2000).
- ⁵⁶V. A. Andronov, S. M. Bakhrakh, V. N. Mokhov, V. V. Nikiforov, and A. V. Pevnitskii, "Effect of turbulent mixing on the compression of laser targets," *JETP Lett.* **29**, 56 (1979).
- ⁵⁷S. Gauthier and M. Bonnet, "A k – ϵ model for turbulent mixing in shock-tube flows induced by Rayleigh–Taylor instability," *Phys. Fluids A* **2**, 1685 (1990).
- ⁵⁸R. D. Blevins, *Applied Fluid Dynamics Handbook* (Van Nostrand Reinhold, New York, 1984), p. 332.
- ⁵⁹E. S. Oran and J. P. Boris, *Numerical Simulation of Reactive Flow*, 2nd ed. (Cambridge University Press, Cambridge, 2001).
- ⁶⁰D. L. Youngs, *Numerical Methods for Fluid Dynamics*, edited by K. W. Morton and M. J. Baines (Academic, London, 1982).
- ⁶¹B. van Leer, "Towards the ultimate conservative difference scheme IV. A new approach to numerical convection," *J. Comput. Phys.* **23**, 276 (1977).
- ⁶²R. B. DeBar, "A method in 2D Eulerian hydrodynamics," Lawrence Livermore National Laboratory Report No. UCID-19683 (1974).
- ⁶³P. Colella and P. Woodward, "The piecewise parabolic method (PPM) for gas-dynamic simulations," *J. Comput. Phys.* **54**, 174 (1984).
- ⁶⁴P. MacNeice, K. M. Olson, C. Mobarry, R. de Fainchtein, and C. Packer, "PARAMESH: A parallel adaptive mesh refinement community toolkit," *Comput. Phys. Commun.* **126**, 330 (2000).
- ⁶⁵W. Gropp, E. Lusk, and A. Skjellum, *Using MPJ: Portable Parallel Programming with the Message Passing Interface*, 2nd ed. (MIT Press, Cambridge, MA, 1999).
- ⁶⁶B. Fryxell, K. Olson, P. Ricker, F. X. Timmes, M. Zingale, D. Q. Lamb, P. MacNiece, R. Rosner, J. W. Truran, and H. Tufo, "FLASH: An adaptive mesh hydrodynamics code for modeling astrophysical thermonuclear flashes," *Astrophys. J., Suppl. Ser.* **131**, 273 (2000).
- ⁶⁷A. C. Calder, L. J. Dursi, B. Fryxell, T. Plewa, V. G. Weirs, T. Dupont, H. F. Robey, J. O. Kane, R. P. Drake, B. A. Remington, G. Dimonte, J. Hayes, J. M. Stone, P. M. Ricker, F. X. Timmes, M. Zingale, and K. Olson, "On validating an astrophysical simulation code," *Astrophys. J., Suppl. Ser.* **143**, 201 (2002).
- ⁶⁸D. H. Porter and P. R. Woodward, "High-resolution simulations of compressible convection using the piecewise-parabolic method," *Astrophys. J., Suppl. Ser.* **93**, 309 (1994).
- ⁶⁹S. K. Godunov, "A difference method for the numerical solution of discontinuities in hydrodynamic equations," *Mathematic Sb.* **47**, 271 (1959) (in Russian).
- ⁷⁰B. van Leer, "Towards the ultimate conservative difference scheme V. A second order sequel to Godunov's method," *J. Comput. Phys.* **32**, 101 (1979).
- ⁷¹M. J. Andrews, "Accurate computation of convective transport in two-phase flow," *Int. J. Numer. Methods Fluids* **21**, 205 (1995).
- ⁷²M. M. Marinak, G. D. Kerbel, N. A. Gentile, O. Jones, D. Munro, S.

- Pollaine, T. R. Dittrich, and S. W. Haan, "Three-dimensional HYDRA simulations of NIF targets," *Phys. Plasmas* **8**, 2275 (2001).
- ⁷³J. S. Peery and D. E. Carroll, "Multimaterial ALE methods in unstructured grids," *Comput. Methods Appl. Mech. Eng.* **187**, 591 (2000).
- ⁷⁴D. L. Youngs, "An interface tracking method for a 3D Eulerian hydrodynamics code," AWE, AWRE/44/92/35, April 1987.
- ⁷⁵A. C. Robinson and J. W. Swegle, "Acceleration instability in elastic-plastic solids. II analytical techniques," *J. Appl. Phys.* **66**, 2859 (1989).
- ⁷⁶B. J. Daly, "Numerical study of two fluid Rayleigh–Taylor instability," *Phys. Fluids* **10**, 297 (1967).
- ⁷⁷M. Wilson and M. J. Andrews, "Spectral measurements of Rayleigh–Taylor mixing at small Atwood number," *Phys. Fluids* **14**, 938 (2002).
- ⁷⁸A. W. Cook and Y. Zhou, "Energy transfer in Rayleigh–Taylor instability," *Phys. Rev. E* **66**, 026312 (2002).
- ⁷⁹D. L. Youngs, "Application of MILES to Rayleigh–Taylor and Richtmyer–Meshkov mixing," AIAA Paper No. 2003-4102 (2003).
- ⁸⁰S. B. Dalziel, P. F. Linden, and D. L. Youngs, "Self-similarity and internal structure of turbulence induced by Rayleigh–Taylor instability," *J. Fluid Mech.* **399**, 1 (1999).